Magnetic Excitations In The Iridate Sr_2IrO_4

by

Andreas Leonhardt

Thesis

for the degree of

Master of Science

Faculty of Mathematics and Natural Sciences
University of Oslo

June 2014

Abstract

In this thesis we investigated magnetic excitations in the iridate compound Sr_2IrO_4 . As a layered strongly correlated system it can be described by the two-dimensional one-band Hubbard model, describing interacting particles in effective spin-$\frac{1}{2}$ states. Based on the previously calculated band structure model, it becomes an effective model with one free parameter, the one-site interaction strength U. Using Green's functions at the mean field level, we calculated the dynamic magnetic susceptibility and thereby the spin wave dispersion. We compared the spin wave dispersion with resonant inelastic X-ray scattering experiments and used it to fit the Hubbard interaction strength U. We found the t-t'-t''-U-Hubbard model based on the band structure energies to provide a good description of the spin wave dispersion for $U = 1.1$eV.

Acknowledgements

Many thanks to my supervisor, Professor Olav Fredrik Syljuåsen, for making this thesis possible. Especially for all the tips and ideas, endurance in finding mistakes and confronting my occasional confusion, and for the fast and flexible revision.

Furthermore, I want to thank my parents a lot for supporting me in every possible way and making my studies in Oslo possible in the first place and enjoyable on top of that. Thank you a lot for backing me all the way, no matter where I go and what I do and giving me the freedom and support to live my life this way.

Thanks to all my friends, who made my time during my masters so much better. Thanks for all the discussions, new experiences and laughters, coffees and beautiful moments we could enjoy together. Special thanks to my fellow students, for making discussions about physics and the world not only instructive, but also entertaining and motivating. Tony, thanks for being both of the above through the whole time and for rocking the final phase together. Thank you Süße for being on my side and being always supportive in stressful times. A special thanks to all my friends for pardoning me ignoring you lately.

Last and least I want to thank Bixit for making great cookies and keeping me somehow nourished on long evenings at the university.

Contents

Chapter 1

Introduction

Transition metal oxides (TMOs) build a class of fascinating materials, whose elements show a variety of condensed matter systems and with multifaceted properties. Various different structures can be realized by choosing the right combination of elements, doping and different preparation techniques. This gives not only the possibility to find practical realizations of theoretical models like low-dimensional systems and spin models, but leads also to the finding of new effects in condensed matter systems. The resulting materials range from metals to insulators, with all sorts of magnetic properties.

The most famous group among them are the cuprates. Their defining component is an anionic complex containing oxidised copper. The discovery of high temperature super conductivity in some of its compounds in 1986 [1] started an era of intensive research on the cuprates that lasts until today.

In the search for interesting physics new classes were created by replacing some of the elements in the compounds, expanding thereby parameter space of defining basic effects to new magnitudes and combinations. The iridates are such a group, where copper in the anionic component is replaced by iridium. While the first components have been synthesized as early as 1969 [2], research on the iridates, both experimentally and theoretically, has intensified greatly in the last decade. Especially since new experimental techniques like resonant inelastic X-ray scattering were discovered, that help to unveil their inner structure.

1.1 Motivation and Goals

We will focus in this thesis on the iridate compound Sr_2IrO_4. Despite intensive research in the last years, there is still ongoing dispute about the exact mechanisms that result in some of its properties.

Sr_2IrO_4 is an insulator, which can not be explained from band structure alone. Possible mechanisms are of the Mott or Slater type [3]. They depend on the strength of SOC and inter-electronic interaction. Especially the strenght of the

interaction is not directly observable and is often only estimated. We use the Hubbard interaction, which is the simplest way of introducing correlations. Its only parameter is the on-site interaction U, which we will determine in this work.

Another interesting property of Sr_2IrO_4 is its weak ferromagnetic moment. The on-site magnetization for this moment is an order of magnitude smaller than what one would expect from atomic states. Furthermore shows the material no ferromagnetic but rather anti-ferromagnetic ordering in the ground state. Due to its canted crystal structure, the ferromagnetic moment can be related to the order parameter of the anti-ferromagnetic ground state. We will determine the order parameter in the ground state, which we can then relate to the measured magnetic moment.

The cuprate La_2CuO_4 is a high temperature superconductor with the same structure as Sr_2IrO_4. Often one chooses a pure spin model to describe their dynamics. A large repulsive interaction justifies this at half filling. In iridates the particle interaction is smaller and the usage of a spin model is not that well justified. We use the Hubbard model based on the band structure instead. We want to show, that the Hubbard model solved at the mean field level is capable of providing a better description of the spin excitations. Sr_2IrO_4 might show superconductivity when doped away from half filling. Understanding the mechanisms defining its basic magnetic excitations might help to find an answer to that question.

1.2 Outline

In the first part of the thesis we will derive the Hubbard model as an effective model for the iridates, starting from its components and the crystal structure. First we describe how effective $J = \frac{1}{2}$ and $J = \frac{3}{2}$ states emerge from the interplay of two effects, the field of the negatively charged oxygen ions and SOC.

We show then how we can create an effective model for the half filled spin-$\frac{1}{2}$ band in the tight binding approximation. We introduce then correlations between electrons, modelled as on-site repulsions. This so called Hubbard interaction is the simplest way of accounting for interactions and has been shown to provide a good description in similar systems, e.g. the cuprates.

We then solve the Hubbard model in the mean field approach. The goal is to calculate the dynamical magnetic susceptibility. From this we can extract the spin wave dispersion, which can be directly compared to results from neutron and X-Ray scattering experiments. We follow the calculation scheme by Peres and Araújo [4] that was used for the structurally similar cuprate La_2CuO_4.

The calculations will first be carried out in the large U limit and compared to the results of linear spin waves in a Heisenberg model. Since the Heisenberg model can be dervied from the Hubbard model in this limit, we can use this to validate the calculations.

We then calculate the dispersion with parameters from Sr_2IrO_4 for different band structures. The results were compared to measurements on this material. The interaction parameter U is the only adjustable parameter in this approach and will be fitted to give the best match to observations. We show that the approach outlined above provides results that agree well with measurements and is capable of reproducing the main features of the dispersion.

Chapter 2

Deriving The Hubbard Model

Iridates is a loosely defined group of TMOs, which contain iridium in its anionic component. A more stringent definition classifies every material containing the salt $(Ir_2O_7)^{6-}$ as iridate. However, the ratio of iridium compared to oxygen might change due to the exact configuration of the component and how many oxygen ions are shared between neighbouring IrO complexes. Its main features are strong electron interactions, which makes it a correlated system as well as strong spin-orbit interactions in iridium. The last property is the most important difference to the otherwise similar cuprates and leads to interesting new physics. In this chapter we will derive an effective model, the one-band Hubbard model. We start from the different constituents and their relative geometrical structure in the crystal and describe the effects of the above mentioned interactions. We show then how we can get orthonormal states based on the previously found atomic states. These states build the basis for the Hubbard model, which is formulated in second quantization.

2.1 Iridates

Iridium is a noble metal and one of the least common metals on earth and its density is among the highest among non-radioactive elements. With an atomic number of 77 it is a transition metal of the platinum group. Transition metals are characterized by a partially filled d-shell , which dominates their chemical behaviour. As part of the heavier elements in the platinum group the d orbitals belong to the 5th shell. Like many transition metals its s-shell of the next atomic number, the $6s$-shell, is filled as well. In the atomic configuration the shell structure is $[\mathrm{Xe}]4f^{14}5d^{7}6s^{2}$. In compounds it can be found in different oxidation states, ranging from -3 to +6. In Sr_2IrO_4 iridium is fourfold oxidized to Ir^{4+}, which removes the $6s^2$ electrons as well as two electrons from the $5d$ shell. The outermost shell is therefore the $5d$ shell, which is half-filled [5].

The other elements of the compounds treated in this thesis are oxygen and

rare earth metals. The oxygen is two fold ionized and has therefore only the closed shells $1s^2, 2s^2, 2p^6$. The same hold for the rare earth metals, strontium is reduced to Sr^{2+} with the electron configuration of Kr. Both the rare earth metal and oxygen have therefore zero total angular momentum and spin.

Iridates show a great variety of geometrical configurations. Important examples are the layered perovskite of the Ruddelson-Popper series of Iridium oxides, $Sr_{n+1}Ir_nO_{3n+1}$ with $n = 1$, honeycomb lattices and more complex three dimensional configuration.

We will focus on Sr_2IrO_4, which belongs to the Ruddelson-Popper series for $n = 1$. n counts the layers that are stacked directly on top of each other, before being separated by Sr ions. Other possible values in this series are 2 and ∞, where the last one means there is no separation any more and we have $SrIrO_3$.

As a layered perovskite, Sr_2IrO_4 consists of single layers with a structure similar to $CaTiO_3$. The latter one is also called perovskite and lends its name to the perovskite structure. It consists of a cubic unit cell, with one type of atom (Ca in perovskite) on the edges, the atom of the other element (Ti) is embedded in an octahedron of oxygen ions, which are located on the face centres, see figure 2.1 for an illustration. In the case of Sr_2IrO_4 it is Ir^{4+} that is located inside the

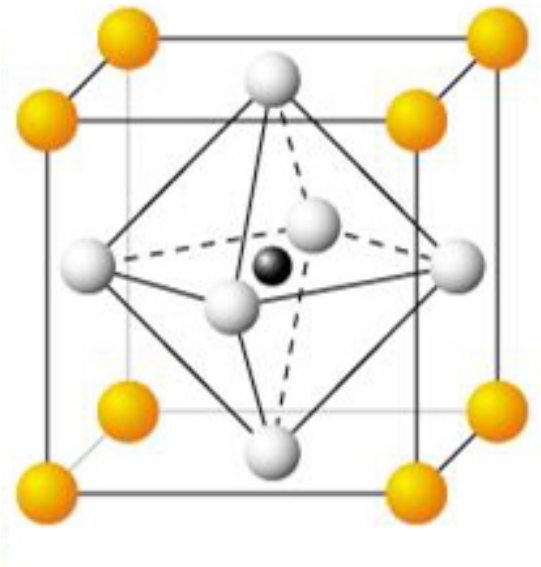

Figure 2.1: Unit cell of a perovskite, the building block of many iridates. The yellow dots represent the rare earth metal, the white dots form the octahedra of the oxygen ligands. The black dot is the iridium ion. Picture taken from [6].

oxygen octahedron. The octahedra share corners in the x-y-direction while being separated by a Sr^{2+} ion in the z-direction. Due to a shift between two subsequent

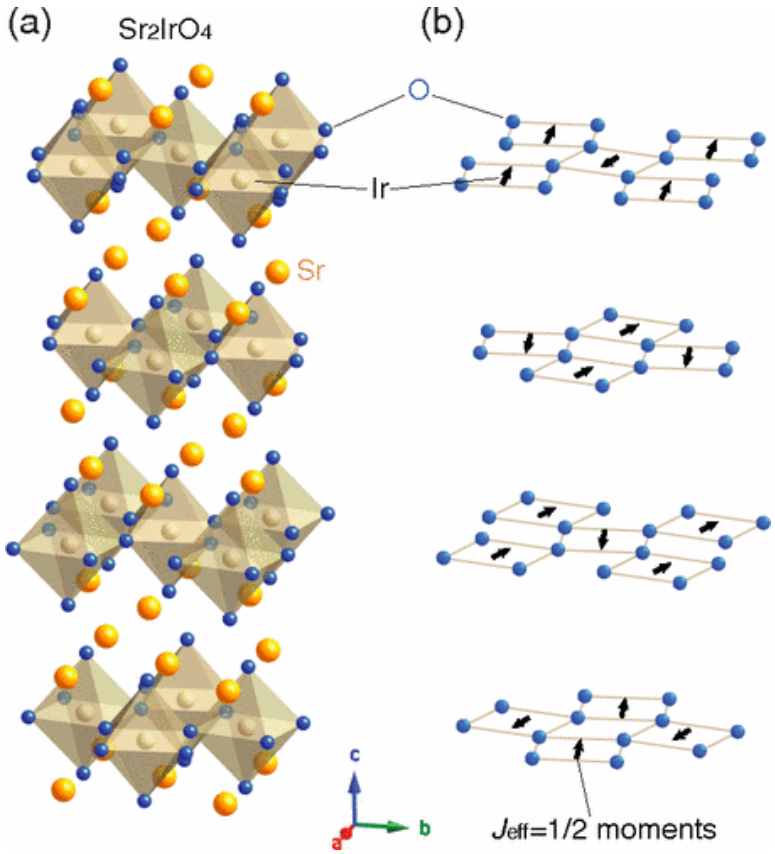

Figure 2.2: a) Tetragonal unit cell of Sr_2IrO_4 . b) Two dimensional layers of perovskite structure
Figure taken from [8].

layers, we have to include two layers in the unit cell in order to regain a cubic one. An octahedron of one layer matches an Sr ion of the other, preventing corner sharing in the z-direction and providing thereby the separation of layers. Furthermore, the octahedra are tilted in a staggered pattern by $\Theta = \pm 11^\circ$ [7]. This enlarges the cubic unit cell to $\sqrt{2}a \times \sqrt{2}b \times 2c$. In x- and y-direction we have to take two iridium ions into the unit cell. The translation vector corresponds now to the former diagonals. At the same time we get four layers in z-direction, until the same pattern of canted octahedra is met again. The unit cell is shown in figure 2.2 We will first neglect the rotations in the further scheme, but discuss the influence it has on the magnetic structure in the final interpretation of response functions. It shows that these rotations are the cause of the small ferromagnetic moment in the otherwise anti-ferromagnetic material.

xy	$\frac{\mathrm{i}}{\sqrt{2}}\left(Y_2^{-2}-Y_2^2\right)$	$\sqrt{\frac{15}{4\pi}}\frac{xy}{r^2}$
xz	$\frac{1}{\sqrt{2}}\left(Y_2^{-1}-Y_2^1\right)$	$\sqrt{\frac{15}{4\pi}}\frac{xz}{r^2}$
yz	$\frac{\mathrm{i}}{\sqrt{2}}\left(Y_2^{-1}+Y_2^1\right)$	$\sqrt{\frac{15}{4\pi}}\frac{yz}{r^2}$
z^2	Y_2^0	$\sqrt{\frac{15}{4\pi}}\frac{3z^2-r^2}{2r^2\sqrt{3}}$
x^2-y^2	$\frac{1}{\sqrt{2}}\left(Y_2^{-2}+Y_2^2\right)$	$\sqrt{\frac{15}{4\pi}}\frac{x^2-y^2}{2r^2}$

Table 2.1: Definition of cubic harmonics of the d orbitals and their relation to the spherical harmonics.

Ligand Field

The $5d$ states in a free iridium ion are degenerate due to rotational symmetry of the atomic Hamiltonian. We choose the cubic harmonics as a basis and denote the states according to their transformation symmetry with respect to the coordinate axes, namely $|x^2-y^2\rangle, |z^2\rangle, |xy\rangle, |xz\rangle$ and $|yz\rangle$. The cubic harmonics are related to the spherical harmonics of the d-orbitals, Y_m^2 for $m=0,\pm1,\pm2$, by a unitarian transformation, shown in table 2.1. As such, the cubic harmonics have all angular momentum $l=2$. and they form an irreducible representation of the rotation group.

Embedding the iridium ion in a crystal breaks the rotational symmetry of the potential due to anisotropic contributions from its neighbours. As a result, the degeneracy of the $5d$ states will be lifted. Since the ion is now surrounded by the ligands in the form of an octahedron, the full rotational symmetry is reduced to the transformation symmetry of the octahedron or equally a cube. These are the 48 transformation of the point group O_h. One can tell from group theory alone, that reducing the symmetry splits an irreducible representation of the rotational group into subgroups, that form irreducible representations corresponding to the lowered symmetry. Comparing the characters of the irreducible presentations for O_h with the ones for the full rotational group SO(3), we find that the latter one has to split up into one two dimensional and one three dimensional subgroup. The degeneracy of the $5d$ states is thereby partially lifted and we get the three-fold degenerate t_{2g} states consisting of the xy, xz, yz orbitals and the two-fold degenerate e_g states formed by z^2 and x^2-y^2 [9, Chapter 4]

The value of the energetic split due to the crystal field depends on the form and strength of the potential generated by the ligands. In Sr_2IrO_4 it is of order $\Delta_c = E(e_g) - E(t_{2g}) \approx 5\text{eV}$ [10]. The sign is such that the e_g states lie at a higher energy than the t_{2g}, which can be understand in an intuitive way from the form of the orbitals. The e_g states fill the space closer to the ligands, requiring therefore energy to overcome the repulsion from the negatively charged oxygen ions, while

the t_{2g} orbitals avoid the ligands by being extended along the diagonals of the unit cell. The large energy split leads to a filling, that breaks Hund's rule, which decreases the inter-particle interaction by filling all orbitals with particles of the same spin, before filling orbitals with two particles of opposite spin. The resulting spatially antisymmetric wave function reduces then the overlap of wave functions.

In the case of iridium we deal with $5d$ states, which are more extended than the $4d$ and $3d$ states of lighter transition metals. This reduces the overall amplitude of the wave function and therefore the repulsion between electrons on different sites. The energy split due to the crystal field is strong enough to favour double occupancies in the t_{2g} states over populating the e_g states. As a result, the e_g states are empty, while all five electrons will be distributed over the t_{2g} states.

2.2 Strong Spin-Orbit Coupling

Until now we neglected interactions between angular momentum and spin. The coupling ζ_{SO} of total angular momentum L and total Spin S is proportional to the charge of the nucleus to the 4th power, Z^4. Spin orbit coupling (SOC) becomes therefore more important in heavier elements and is no longer negligible in iridates. Strong SOC is the main difference between iridates and cuprates. It is the cause of interesting new effects like the insulating behaviour up to high temperatures.

The total effective angular momentum of the t_{2g}-states is $L = 1$. There are five electrons in the three states, leaving one hole. Due to the Pauli principle, only three electrons can have the same spin, the other two must have the opposite spin. The total spin S adds therefore up to $\frac{1}{2}$. The total angular momentum and total spin can then be coupled to $J = \frac{3}{2}$ and $J = \frac{1}{2}$. SOC accounted for by adding the term $\zeta_{\mathrm{SO}} \sum_i \hat{\mathbf{L}} \cdot \hat{\mathbf{S}}$ to the Hamiltonian, where ζ_{SO} denotes the coupling strength. Its value in Sr_2IrO_4 is given by $\zeta_{\mathrm{SO}} = 0.37\mathrm{eV}$ [11].

The matrix elements of the interaction term in the cubic harmonics basis are given by

$$\langle \alpha, \sigma | \, \hat{\mathbf{L}} \cdot \hat{\mathbf{S}} \, | \beta, \sigma' \rangle = \sum_{j=x,y,z} \langle \alpha | \, \hat{L}_j \, | \beta \rangle \, \langle \sigma | \, \hat{S}_j \, | \sigma' \rangle \tag{2.1}$$

with $\alpha, \beta \in \{xy, xz, zy\}$ and the spin values $\sigma, \sigma' \in \{\uparrow, \downarrow\}$. The angular momentum matrix elements can be easily calculated by the substitution $L_x = \frac{1}{2}(L^+ + L^-)$ and $L_y = \frac{-\mathrm{i}}{2}(L^+ - L^-)$. and expressing the t_{2g}-states through the spherical harmonics. The components of the angular momentum operators act on the spherical harmonics through $L_z Y_l^m = m Y_l^m$, $L^+ Y_l^m = \sqrt{(l-m)(l+m+1)} Y_l^{m+1}$ and $L^- Y_l^m = \sqrt{(l+m)(l-m+1)} Y_l^{m-1}$. The spin operator is proportional to the Pauli matrices, $\tau_j = \frac{1}{2}\sigma_j$. We are left with a hermitian matrix with only six

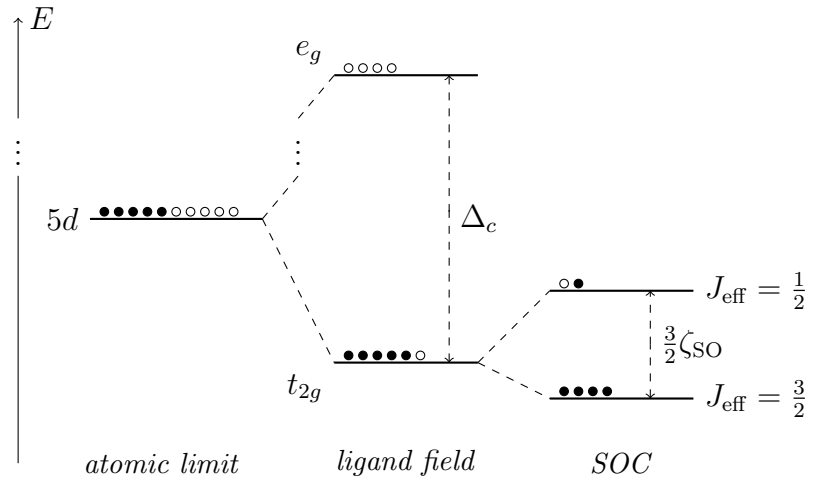

Figure 2.3: scheme of the split-up of states due to the crystal field and spin orbit coupling. The circles indicate the available spaces and are filled if occupied.

independent, non-zero components, namely

$$\begin{aligned}
\langle zx,\sigma|\,\hat{\mathbf{L}}\cdot\hat{\mathbf{S}}\,|xy,-\sigma\rangle &= \frac{\mathrm{i}\zeta_{\text{SO}}}{2}\\
\langle yz,\sigma|\,\hat{\mathbf{L}}\cdot\hat{\mathbf{S}}\,|xy,-\sigma\rangle &= -s_\sigma\frac{\zeta_{\text{SO}}}{2}\\
\langle zx,\sigma|\,\hat{\mathbf{L}}\cdot\hat{\mathbf{S}}\,|zx,\sigma\rangle &= s_\sigma\frac{\mathrm{i}\zeta_{\text{SO}}}{2},
\end{aligned} \tag{2.2}$$

where $s_\uparrow = +1$, $s_\downarrow = -1$ denote the signs of the spins. This matrix has two eigenvalues, $-\zeta_{\text{SO}}/2$ and $+\zeta_{\text{SO}}$. The subspace for the lower one is 4 dimensional and corresponds to the $J_{\text{eff}} = \frac{3}{2}$ state, the other one is the two-dimensional $J_{\text{eff}} = \frac{1}{2}$ subspace. In the ground state the $J = \frac{3}{2}$ band will be completely occupied, while the $J = \frac{1}{2}$ band is half-filled. Figure 2.3 shows the energetic split and the occupancy of energy levels in the ground state.

The two eigenstates of $J_{\text{eff}} = \frac{1}{2}$ are given by a linear combination of the molecular orbitals and spin states,

$$\left|J_{\text{eff}} = \frac{1}{2}, M_{J_{\text{eff}}} = \sigma\right\rangle = \frac{1}{\sqrt{3}}\left(|yz,\sigma\rangle - s_\sigma\mathrm{i}\,|zx,\sigma\rangle - s_\sigma\,|xy,-\sigma\rangle\right). \tag{2.3}$$

2.3 Tight Binding Model

So far we considered only ions and their immediate vicinity in the limit of infinite separation from each other, i.e. without the influence of a crystal pattern and interactions between different sites of the lattice. In reality the orbitals constructed

above show some overlap, which creates the possibility of transitions and interactions between neighbouring sites. In this chapter we show, that it is possible to construct a set of localized orthonormal states based on atomic states. This allows us then to describe the system using second quantization.

Electrons in iridates are localized, i.e. they are well described by wave functions which are centred around sites in the crystal and fall off fast as one is moving further away. Atomic orbitals provide a good starting point for this case.

We denote the nth orbital of the unit cell at site $\mathbf{R}_i$ with $|\phi_I\rangle = \phi^n(\mathbf{r} - \mathbf{R}_i)$. $I = (n, i)$ is the combined index of orbital number n and site number i. n runs over the relevant orbitals of all atoms in the unit cell. Even though the orbitals are localized, we have a non-zero overlap for different $I = (i, n)$ and $J = (j, m)$, $\langle\phi_I|\phi_J\rangle = S_{IJ} \neq \delta_{IJ}$. This includes overlaps in the unit cell and across sites. The potential in the Hamiltonian is now the sum over atomic potentials at all sites, and the total single-particle Hamiltonian reads

$$\begin{aligned}\hat{H} &= \frac{1}{2m}\nabla^2 - \sum_I V^n_{\text{atom}}(\mathbf{r} - \mathbf{R}_i) \\ &= H^n_{\text{atom}}(\mathbf{R}_i) - \sum_{J\neq I} V^m_{\text{atom}}(\mathbf{r} - \mathbf{R}_j)\end{aligned} \tag{2.4}$$

In the last line we grouped the terms belonging to the single atom Hamiltonian at space $\mathbf{R}_i$, of which $|\phi_I\rangle$ is an eigenfunction with eigenvalue E^n. This allows us to easily identify different contributions the matrix elements of the Hamiltonian.

$$\langle\phi_I|\,\hat{H}\,|\phi_J\rangle = E^n\mathbf{S}_{IJ} - \beta^m\delta_{IJ} - \mathbf{T}_{IJ} \tag{2.5}$$

β^m corresponds to a shift of energy, due to the integral over the atomic potentials located on all sites apart I,

$$\beta^m = \int \mathrm{d}^3r\ \phi^n(\mathbf{r} - \mathbf{R}_i)^* \sum_{I'\neq I} V^{n'}_{\text{atom}}(\mathbf{r} - \mathbf{R}_{i'})\phi^n(\mathbf{r} - \mathbf{R}_i) \tag{2.6}$$

This contribution will be small, since $\phi^n(\mathbf{r} - \mathbf{R}_i)$ is small outside the unit cell at $\mathbf{R}_i$. The matrix $\mathbf{T}_{IJ}$ consists of all non-diagonal integrals of this type,

$$\mathbf{T}_{IJ} = \int \mathrm{d}^3r\ \phi^{n*}(\mathbf{r} - \mathbf{R}_i) \sum_{I'\neq I} V^{n'}_{\text{atom}}(\mathbf{r} - \mathbf{R}_{i'})\phi^m(\mathbf{r} - \mathbf{R}_j) \tag{2.7}$$

if $I \neq J$ and 0 otherwise. The biggest contribution in the sum comes from the term with $I' = J$, since one wave function has a central overlap with the potential.

We want to transform our basis states such that they are orthonormal but still located around lattice sites. Functions of this type are the Wannier functions Ψ_I. They are given by the Fourier transformation of Bloch functions. We introduce a combined index for k-space as well, $K = (n, \mathbf{k})$. Changing to Fourier space is a

unitary operation that can be expressed in matrix notation. The transformation matrix $\mathbf{U}$ is defined through $\mathbf{U}_{IK} = N^{-\frac{1}{2}} \mathrm{e}^{\mathrm{i}\mathbf{k}\mathbf{R}_i} \delta_{nm}$. and we can write

$$\Psi_I(\mathbf{r}) = \frac{1}{\sqrt{N}} \sum_{\mathbf{k}} \mathrm{e}^{\mathrm{i}\mathbf{k}\mathbf{R}_i} \Psi_K(\mathbf{r}) = \sum_K \mathbf{U}_{IK} \Psi_K(\mathbf{r}) \tag{2.8}$$

Bloch functions are eigenfunctions of the translation operator of the lattice. Under a symmetry translation of the lattice, they will only pick up a phase,

$$\Psi_K(\mathbf{r} + \mathbf{T}) = \mathrm{e}^{\mathrm{i}\mathbf{k}\mathbf{T}} u_K(\mathbf{r}). \tag{2.9}$$

$\mathbf{T}$ is a translation vector of the lattice and $u_K(\mathbf{r})$ is a function with the same periodicity as the lattice. As eigenfunctions the Bloch states are orthogonal, which can also be seen by the completeness relation of $\sum_i \mathrm{e}^{\mathrm{i}(\mathbf{k}-\mathbf{k}')\mathbf{R}_i} = N\delta(\mathbf{k}-\mathbf{k}')$ Since the transformation to Wannier states is a unitary transformation, e.g. $\mathbf{U}^\dagger = \mathbf{U}^{-1}$, it follows immediately that they are orthogonal as well.

We can now construct Bloch functions from the atomic functions by means of Bloch sums.

$$\Psi_K(\mathbf{r}) = N_K \sum_i \mathrm{e}^{\mathrm{i}\mathbf{k}\mathbf{R}_i} \phi^n(\mathbf{r} - \mathbf{R}_i). \tag{2.10}$$

N_K is a k- and n-dependent normalization factor

$$\begin{aligned} N_K^{-2} &= \sum_{i,j} \mathrm{e}^{\mathrm{i}\mathbf{k}(\mathbf{R}_i - \mathbf{R}_j)} \int \mathrm{d}^3 r \phi^{n*}(\mathbf{r} - \mathbf{R}_i) \phi^n(\mathbf{r} - \mathbf{R}_j) \\ &= \sum_{IJ} \mathbf{U}^\dagger_{KI} S_{IJ} \mathbf{U}_{JK} \end{aligned} \tag{2.11}$$

Constructed in this way, the states fulfil the requirement of 2.9, since

$$\begin{aligned} \Psi_K(\mathbf{r} + \mathbf{T}) &= N_K \mathrm{e}^{\mathrm{i}\mathbf{k}\mathbf{T}} \sum_i \mathrm{e}^{\mathrm{i}\mathbf{k}(\mathbf{R}_i - \mathbf{T})} \phi^n(\mathbf{r} - \mathbf{R}_i + \mathbf{T}) \\ &= N_K \mathrm{e}^{\mathrm{i}\mathbf{k}\mathbf{T}} \sum_i \mathrm{e}^{\mathrm{i}\mathbf{k}\mathbf{R}_i} \phi^n(\mathbf{r} - \mathbf{R}_i), \end{aligned} \tag{2.12}$$

where the second step is simply done by a shift in the sum. Using the Bloch sums to construct Wannier functions yields the states we are looking for. These so called Löwdin orbitals are given by

$$|\varphi_I\rangle = \sum_j \sum_{\mathbf{k}} \mathrm{e}^{\mathrm{i}\mathbf{k}(\mathbf{R}_i - \mathbf{R}_j)} N_k |\phi_J\rangle \delta_{mn} = \sum_J \left(\mathbf{U} (\mathbf{U}^* \mathbf{S} \mathbf{U})^{-\frac{1}{2}} \mathbf{U}^* \right)_{IJ} |\phi_J\rangle \delta_{mn} \tag{2.13}$$

Finally, we can express the Löwdin states in term of atomic orbitals and their overlaps,

$$|\varphi_I\rangle = \sum_J (\mathbf{S}^{-\frac{1}{2}})_{IJ} |\phi_J\rangle \delta_{mn}. \tag{2.14}$$

The matrix $\mathbf{S}^{-\frac{1}{2}}$ is defined by a Taylor series of the matrix $\mathbf{S}$. Therefore commute $\mathbf{S}$ and its square root and it follows that$\mathbf{S}^{-\frac{1}{2}}$ is hermitian as well. Since we have only small off-diagonal elements and 1 on the diagonal, we see that the Löwdin states are still localized around the centres. In the limit of large separations, $\mathbf{S}$ approaches the identity, and we regain the atomic orbitals. The main difference between the Löwdin states and the atomic ones are oscillations of the phase, that ensure orthogonality.

We can now express the matrix elements of the Hamiltonian in the new basis.

$$\langle \varphi_I | \hat{H} | \varphi_J \rangle = (E^m - \beta^m)\delta_{IJ} - t_{IJ} \tag{2.15}$$

$$t_{IJ} = \begin{cases} -\beta \mathbf{S}_{IJ} - (\mathbf{S}^{-\frac{1}{2}} \mathbf{T} \mathbf{S}^{-\frac{1}{2}})_{IJ} & I \neq J \\ 0 & I = J \end{cases}$$

The calculation of t_{IJ} requires detailed knowledge about the atomic states and the periodic potential. They are usually calculated through other approximation schemes, for example the local density approximation (LDA). In calculations we will use values from the literature, that were fitted to LDA + SO calculations.

2.3.1 Superexchange

The direct hopping terms between iridium orbitals are negligible, since the iridium sites are separated by oxygen ions and the overlaps of orbitals from two different iridium atoms are negligible. Transitions between iridium sites are still possible, when they are mediated through the p-orbitals of oxygen ions. These two step hopping processes are called super exchange and give rise to an antiferromagnetic coupling. We will just sketch how to calculate the main contribution to an effective Ir-Ir hopping.

The oxygen ion between two iridium atoms has completely filled p-orbitals, one of which is aligned along the line connecting the two iridium sites. Hopping to and from this orbital gives the most important contribution, while transitions between p-orbitals are forbidden. We denote the parameter for hopping from an iridium orbital to the oxygen orbital by t_p. A scheme of the processes leading to super exchange can be seen in figure 2.4. Since this involves two hopping processes, to and from the p-orbital, we get two factors of t_p. Projecting the oxygen states out leads to an additional factor of $\frac{1}{E}$ where $E = U + (E_d - E_p)$ is the energy of the intermediate step, given by the energies of the p and d states plus an energy due to the repulsion between two electrons in the d orbital. The effective hopping is then $t = \frac{t_p^2}{U + E_d - E_p}$.

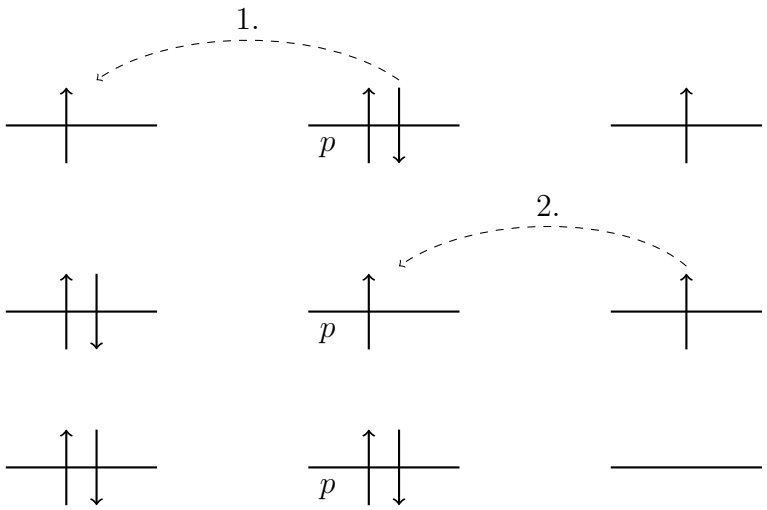

Figure 2.4: scheme of the two processes involved in superexchange hopping between two iridium sites, mediated through a p-orbital from the ligands

2.4 Second Quantization

Having defined our single particle Hamiltonian in terms of orthonormal wave orbitals, we can construct the many particle wave function in terms of creation and annihilation operators. The operator $c^\dagger_{i,\sigma}$ creates a particle with spin σ in the orbital $|\varphi_i\rangle$, while its hermitian conjugate $c_{i,\dagger}$ removes it. They have to fulfil the anti-commutation rules for fermions,

$$\begin{aligned} \left\{c^\dagger_{i,\sigma}\ ,\ c_{j,\sigma'}\right\} &= \delta_{ij}\delta_{\sigma,\sigma'} \qquad \left\{c_{i,\sigma}\ ,\ c_{j,\sigma'}\right\} = 0 \\ \left\{c^\dagger_{i,\sigma}\ ,\ c^\dagger_{j,\sigma'}\right\} &= 0 \end{aligned} \tag{2.16}$$

It follows immediately that $-c^\dagger_{i,\sigma}c^\dagger_{j,\sigma} = c^\dagger_{j,\sigma}c^\dagger_{i,\sigma}$ and $(c^\dagger_{i,\sigma})^2 = 0$. These relations ensure the antisymmetry of the total wave function and thereby the Pauli principle.

Creation and annihilation operators can be translated to momentum space as well. The operators $c^\dagger_{\mathbf{k},\sigma}$ and $c_{\mathbf{k},\sigma}$ represent then the creation and annihilation of a particle with spin σ in the Wannier state $|\Psi_\mathbf{k}\rangle$.

$$\begin{aligned} c^\dagger_{i,\sigma} &= \frac{1}{\sqrt{N}}\sum_\mathbf{k} \mathrm{e}^{\mathrm{i}\mathbf{k}\mathbf{R}_i}c^\dagger_{\mathbf{k},\sigma}, \quad c_{i,\sigma} = \frac{1}{\sqrt{N}}\sum_\mathbf{k} \mathrm{e}^{-\mathrm{i}\mathbf{k}\mathbf{R}_i}c_{\mathbf{k},\sigma}, \\ c^\dagger_{\mathbf{k},\sigma} &= \frac{1}{\sqrt{N}}\sum_i \mathrm{e}^{-\mathrm{i}\mathbf{k}\mathbf{R}_i}c^\dagger_{i,\sigma}, \quad c_{\mathbf{k},\sigma} = \frac{1}{\sqrt{N}}\sum_i \mathrm{e}^{\mathrm{i}\mathbf{k}\mathbf{R}_i}c_{i,\sigma}. \end{aligned} \tag{2.17}$$

They fulfil the same anti-commutation rules as the operators in real space, e.g. the only non-zero anti-commutator is $\{c^\dagger_{\mathbf{k},\sigma}, c_{\mathbf{k}',\sigma'}\} = \delta_{\mathbf{k}\mathbf{k}'}\delta_{\sigma\sigma'}$.

The single particle Hamiltonian, from now on denoted by $\hat{H}_0$, reads in second quantization

$$\hat{H}_0 = \sum_{\sigma} \sum_{ij} -t_{ij}\, c^{\dagger}_{i,\sigma} c_{j,\sigma}, \tag{2.18}$$

where t_{ij} are the off-diagonal matrix elements $\langle \varphi_i | \, \hat{H} \, | \varphi_j \rangle$ defined above.

In cases where the tight binding approximation is valid, these hopping terms might be very small for large distances between site i and j. As a simplification we restrict the model to close neighbours only, setting all other elements of t_{ij} to zero. More precisely, we will restrict ourselves to first, second and third nearest neighbours only. Due to translational invariance, t_{ij} depends only on the relative distance $\mathbf{R}_i - \mathbf{R}_j$ between two sites. We further assume isotropy between neighbours in different directions but with the same distance. Then, t_{ij} depends only on three parameters,

$$t_{ij} = \begin{cases} t & \text{for } \langle i,j \rangle, \quad \text{nearest neighbours} \\ t' & \text{for } \langle\langle i,j \rangle\rangle, \quad \text{next nearest neighbours} \\ t'' & \text{for } \langle\langle\langle i,j \rangle\rangle\rangle, \quad \text{next to next nearest neighbours} \\ 0 & \text{otherwise} \end{cases} \tag{2.19}$$

and we can restrict the double sum over all pairs to neighbouring pairs with a non-zero contribution only.

$$\begin{aligned} \hat{H}_0 = -t \sum_{\langle i,j \rangle, \sigma} \left(c^{\dagger}_{i,\sigma} c_{j,\sigma} + c^{\dagger}_{j,\sigma} c_{i,\sigma} \right) - t' \sum_{\langle\langle i,j \rangle\rangle, \sigma} \left(c^{\dagger}_{i,\sigma} c_{j,\sigma} + c^{\dagger}_{j,\sigma} c_{i,\sigma} \right) \\ -t'' \sum_{\langle\langle\langle i,j \rangle\rangle\rangle, \sigma} \left(c^{\dagger}_{i,\sigma} c_{j,\sigma} + c^{\dagger}_{j,\sigma} c_{i,\sigma} \right) - \mu \sum_{i,\sigma} c^{\dagger}_{i,\sigma} c_{i;\sigma} \end{aligned} \tag{2.20}$$

The sums are restricted such that each pair i, j is counted only once.

2.5 Band Structure In Momentum Space

In the simplest version only nearest neighbour hopping is taken into account, setting t' and t'' to zero as well.

$$\hat{H}_0 = -t \sum_{\langle i,j \rangle, \sigma} \left(c^{\dagger}_{i,\sigma} c_{j,\sigma} + c^{\dagger}_{j,\sigma} c_{i,\sigma} \right) - \mu \sum_{i,\sigma} c^{\dagger}_{i,\sigma} c_{i,\sigma} \tag{2.21}$$

In the second term we introduced the chemical potential. It shows the energetic cost to add a particle to the system. We use it here as an external parameter

that can be used to control the particle density n, the number of particles per site. n ranges from 0 to 2, since maximally two particles with opposite spin can occupy each state.

In order to represent the Hamiltonian in momentum space we insert the relation between the representation of creation and annihilation operators in real space and momentum space, Eq. (2.17). First, we have a look at the chemical potential term. Because of the completeness relation $\sum_i \mathrm{e}^{(\mathbf{k}-\mathbf{l})\mathbf{R}_i} = N\delta_{\mathbf{kl}}$, it is diagonal in k-space

$$-\mu \sum_{i,\sigma} c^\dagger_{i,\sigma} c_{i,\sigma} = -\mu \sum_{\mathbf{k},\sigma} c^\dagger_{\mathbf{k},\sigma} c_{\mathbf{k}\sigma}. \tag{2.22}$$

In a similar manner the hopping term turns into

$$-\frac{t}{N} \sum_{\mathbf{kl},\sigma} \sum_{\langle i,j\rangle} \left(\mathrm{e}^{-\mathrm{i}(\mathbf{k}\mathbf{R}_i - \mathbf{l}\mathbf{R}_j)} c^\dagger_{\mathbf{k},\sigma} c_{\mathbf{l},\sigma} + \mathrm{e}^{-\mathrm{i}(\mathbf{k}\mathbf{R}_j - \mathbf{l}\mathbf{R}_i)} c^\dagger_{\mathbf{k},\sigma} c_{\mathbf{l},\sigma} \right). \tag{2.23}$$

We can now re-parametrize the sum over nearest neighbours, using the translation vectors $\mathbf{T}_d$ between nearest neighbours. d is an index, that runs over all nearest neighbours.

$$\sum_{\langle i,j\rangle} = \sum_i \sum_d \quad ; \quad \mathbf{R}_j = \mathbf{R}_i + \mathbf{T}_d \tag{2.24}$$

We can therefore write 2.23 as

$$\begin{aligned} &-\frac{t}{N} \sum_{\mathbf{k},\mathbf{l},\sigma} \sum_i \mathrm{e}^{-\mathrm{i}(\mathbf{k}-\mathbf{l})\mathbf{R}_i} \sum_d \left(\mathrm{e}^{-\mathrm{i}\mathbf{k}\mathbf{T}_d} + \mathrm{e}^{\mathrm{i}\mathbf{l}\mathbf{T}_d} \right) c^\dagger_{\mathbf{k},\sigma} c_{\mathbf{l},\sigma} \\ &= \sum_{\mathbf{k},\sigma} c^\dagger_{\mathbf{k},\sigma} c_{\mathbf{k},\sigma} \underbrace{\sum_d -2t \cos(\mathbf{k}\mathbf{T}_d)}_{\varepsilon_{\mathbf{k}}} \end{aligned} \tag{2.25}$$

which shows that the single-particle Hamiltonian is diagonal in momentum space with the Wannier functions as eigenstates and momentum dependent eigenvalues $\varepsilon_{\mathbf{k}}$.

In the case of a two dimensional square lattice, the translational vectors of nearest neighbours are given by the lattice constant a times the unit vectors in x- and y-direction, $T_d = a \cdot \mathbf{e}_d$, $d \in \{x, y\}$, shown as green arrows in figure 2.5. Using a as the basic length unit, that is $a = 1$, and normalizing therefore the momentum to the interval $[-\pi, \pi] \times [-\pi, \pi]$ we get in this case

$$\varepsilon_{\mathbf{k}} = -2t \cos(k_x) - 2t \cos(k_y). \tag{2.26}$$

The additional term one gets for non-zero second and third neighbour interactions can be treated the same way. One has to include the corresponding translational vectors $\mathbf{T}_d$ with their respective couplings. Figure 2.5 shows the vectors up to third neighbour interactions in the 2D square lattice. The third

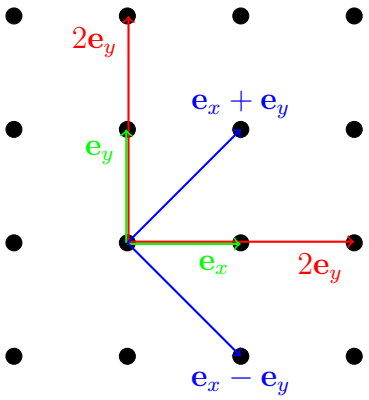

Figure 2.5: Translation vectors $\mathbf{T}_d$ in a two dimensional square lattice for first (green), second (blue) and third (red) neighbour interactions.

neighbours have the same type of translational vectors as the first neighbours, just with twice the length. The second neighbours are found at $\mathbf{e}_x \pm \mathbf{e}_y$. The resulting expression for the energy dispersion in this situation reads

$$\varepsilon_{\mathbf{k}} = -2t\,(\cos k_x + \cos k_y) - 4t' \cos k_x \cos k_y - 2t''\,(\cos 2k_x + \cos 2k_y) \tag{2.27}$$

We note that the hopping term represents the kinetic energy of particles moving between different sites. It is the hopping parameter and the geometry of the lattice, that provide the energy dispersion. The energy dispersion for Sr_2IrO_4 with and without next-to-nearest neighbour interactions are shown in figure 2.6.

2.6 Hubbard Interaction

So far we did not take any interactions between particles into account. The general form of a two particle operator is

$$H_{\text{int}} = \sum_{\sigma_1\sigma_2\sigma_3\sigma_4} \sum_{ijkl} U_{ijkl}\, c^\dagger_{i,\sigma_1} c^\dagger_{j,\sigma_2} c_{k,\sigma_3} c_{l,\sigma_4} \tag{2.28}$$

The matrix elements U_{ijkl} are independent of spin and given by

$$U_{ijkl} = \int \mathrm{d}^3r\, \mathrm{d}^3r'\, \varphi_i^*(\mathbf{r})\varphi_j^*(\mathbf{r}') \frac{e^2}{|\mathbf{r}-\mathbf{r}'|} \varphi_k(\mathbf{r})\varphi_l(\mathbf{r}) \tag{2.29}$$

Due to the small overlap of different states φ_i, only a few matrix elements are important. The diagonal matrix elements $U_{iiii} = U$ account for the repulsion between electrons on the same site and are certainly the most important contribution. From the fermionic commutation relations we know that $c^{\dagger 2}_{\mathbf{k},\sigma} = c^2_{\mathbf{k},\sigma} = 0$.

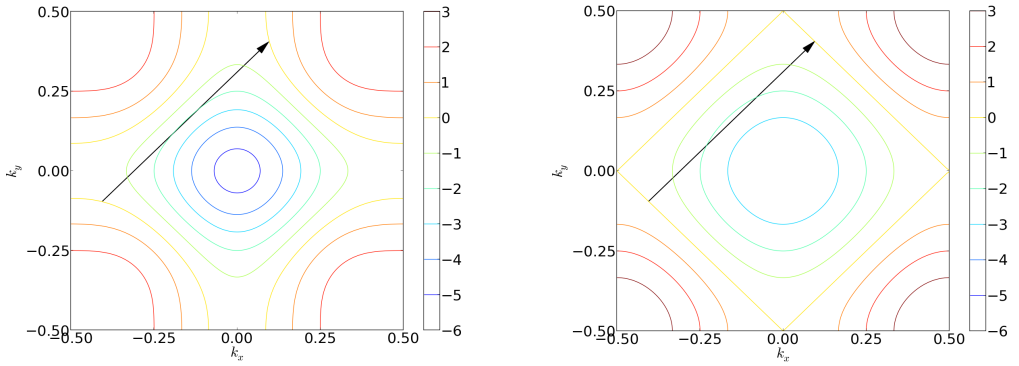

(a) $t' = t'' = 0$ **(b)** $t' = 0.2326t$, $t'' = 0.1163t$

Figure 2.6: Contour plots of the single particle energy dispersion in units of t. Momenta are given in units of 2π. The arrow is a vector, called the nesting vector **Q**, that connects large parts of the Fermi surface. This symmetry leads to an anti-ferromagnetic ground state.

The only non-zero term proportional to U_{iiii} is therefore $c^\dagger_{i,\uparrow} c^\dagger_{i,\downarrow} c_{i,\uparrow} c_{i,\downarrow}$. Using the number operator $n_{i,\sigma} = c^\dagger_{i,\sigma} c_{i,\sigma}$, the diagonal interaction term reads

$$H_{\text{int}} = U \sum_i n_{i,\uparrow} n_{i,\downarrow}. \tag{2.30}$$

Other terms count the interaction of density fluctuations at neighbouring sites through U_{ijij} or the exchange coupling U_{ijji}, which yields a Heisenberg like coupling J_{ij}.

In the Hubbard model however we take only the diagonal terms U_{iiii} into account. We choose therefore $U_{ijkl} = \delta_{ijkl} U$. Reducing an interaction that is not necessarily local to only on-site interactions is a grave simplification, neglecting the vast amount of parameters in the interaction matrix U_{ijkl} and therefore long range repulsion and exchange effects. As a result, the optimal value for U, the only parameter left, does not any longer depend on the integral given above in a simple way. The interaction seems to be drastically lowered due to screening effects compared to the value one would expect from the correlation integral of the corresponding orbitals [12]. It is not possible to link the parameter U to a physical quantity directly and the Hubbard model is therefore not a first principle model. U will be treated as an effective parameter and chosen in order to describe the observed behaviour correctly.

2.6.1 Hubbard Term In Momentum Space

We can express the interaction term through creation and annihilation operators in momentum space as well. The summation over all sites in the transformation

yields an overall δ-function of momenta,

$$\begin{aligned}
&\frac{U}{N^2}\sum_{\mathbf{klmn}}\sum_{i}\mathrm{e}^{-\mathrm{i}(\mathbf{k}-\mathbf{l}+\mathbf{m}-\mathbf{n})\mathbf{R}_i}c^{\dagger}_{\mathbf{k},\uparrow}c_{\mathbf{l},\uparrow}c^{\dagger}_{\mathbf{m},\downarrow}c_{\mathbf{n},\downarrow}\\
=&\frac{U}{N}\sum_{\mathbf{klmn}}\delta(\mathbf{k}-\mathbf{l}+\mathbf{m}-\mathbf{n})c^{\dagger}_{\mathbf{k},\uparrow}c_{\mathbf{l},\uparrow}c^{\dagger}_{\mathbf{m},\downarrow}c_{\mathbf{n},\downarrow}\\
=&\frac{U}{N}\sum_{\mathbf{kk'q}}c^{\dagger}_{\mathbf{k},\uparrow}c_{\mathbf{k}-\mathbf{q},\uparrow}c^{\dagger}_{\mathbf{k'},\downarrow}c_{\mathbf{k'}+\mathbf{q},\downarrow}\,. \qquad (2.31)
\end{aligned}$$

In the last line we choose a convenient parametrization of momenta. The interaction is non-diagonal, but it ensures momentum conversation at each vertex.

The total expression for the Hamiltonian in momentum space reads

$$\hat{H}=\sum_{\mathbf{k},\sigma}\left(\varepsilon_{\mathbf{k}}-\mu\right)c^{\dagger}_{\mathbf{k},\sigma}c_{\mathbf{k},\sigma}+\frac{U}{N}\sum_{\mathbf{kk'q}}c^{\dagger}_{\mathbf{k},\uparrow}c_{\mathbf{k}-\mathbf{q},\uparrow}c^{\dagger}_{\mathbf{k'},\downarrow}c_{\mathbf{k'}+\mathbf{q},\downarrow} \qquad (2.32)$$

Chapter 3

Solving The Hubbard Model

3.1 Mean Field Equations

The Mean Field Hamiltonian

We treat the Hubbard model in a perturbative approach at the mean field level. The Hubbard term H_U represents the perturbation. The two-particle operator can be written as a product of two single particle operators. We can rewrite any product of two operators $\hat{A}$ and $\hat{B}$ as

$$\hat{A} \cdot \hat{B} = \left(\hat{A} - \langle\hat{A}\rangle\right)\left(\hat{B} - \langle\hat{B}\rangle\right) + \langle\hat{A}\rangle\hat{B} + \langle\hat{B}\rangle\hat{A} - \langle\hat{A}\rangle\langle\hat{B}\rangle \tag{3.1}$$

In the mean field approach we neglect the first term on the right hand side –the product of fluctuations around their expectation value– leaving us with

$$\hat{A} \cdot \hat{B} \approx \langle\hat{A}\rangle\hat{B} + \langle\hat{B}\rangle\hat{A} - \langle\hat{A}\rangle\langle\hat{B}\rangle \tag{3.2}$$

We use this relation on the single particle operators $c^\dagger_{\mathbf{k},\uparrow}c_{\mathbf{k}-\mathbf{q},\uparrow}$ and $c^\dagger_{\mathbf{k},\downarrow}c_{\mathbf{k}+\mathbf{q},\downarrow}$ in the Hubbard term of the Hamiltonian. Furthermore, we drop the constant term corresponding to $\langle\hat{A}\rangle\langle\hat{B}\rangle$, since a constant in the Hamiltonian will not have any influence on the dynamics of the system. The mean field approximation of the Hubbard term reads

$$H_U \overset{\text{mf}}{\approx} \frac{U}{N}\sum_{\mathbf{q}}\sum_{\sigma}\left(\sum_{\mathbf{p}'}\langle c^\dagger_{\mathbf{p}',-\sigma}c_{\mathbf{p}'+\mathbf{q},-\sigma}\rangle\right)\sum_{\mathbf{p}} c^\dagger_{\mathbf{p},\sigma}c_{\mathbf{p}-\mathbf{q},\sigma}. \tag{3.3}$$

The expectation value for the one particle operator is different from zero for only two values of $\mathbf{q}$. First, for $\mathbf{q} = 0$ the expression yields the spin dependent filling factor, i.e. the number of particles with spin σ relative to the total number of sites N.

$$n_\sigma = \frac{1}{N}\sum_{\mathbf{k}}\langle c^\dagger_{\mathbf{k},\sigma}c_{\mathbf{k},\sigma}\rangle. \tag{3.4}$$

A single site can be empty or occupied by one particle at a given spin σ. The possible values for n_σ are therefore restricted to the range $[0, 1]$. The total number density is simply the sum of both spin dependent number densities, $n = n_\uparrow + n_\downarrow$ and ranges from the empty case $n = 0$ to 2, corresponding to a situation where each site is occupied by two particles with opposite spin.

The second contribution comes from $\mathbf{q} = (\frac{1}{2}, \frac{1}{2})$ in units of $\frac{2\pi}{a}$, which we will use as the momentum unit throughout the whole thesis. This vector acts as a nesting vector $\mathbf{Q}$ for the Fermi surface of the band structure. This means that large parts of the Fermi surface can be mapped onto itself by a translation of this vector.

The dispersion of a square lattice with only nearest-neighbour interactions depends only on $\cos(k_x) + \cos(k_y)$. and is therefore perfectly nested. That means $\varepsilon_{\mathbf{k}} = -\varepsilon_{\mathbf{k}+\mathbf{Q}}$. The Fermi surface at half filling is in this case a perfect square. Introducing higher order hopping terms deforms the Fermi surface, but nesting with $\mathbf{Q}$ holds on a approximate level for small t' and t''. The Fermi surfaces together with the nesting vector $\mathbf{Q}$ are shown for both cases in figure 2.6.

Nesting with $\mathbf{Q} = (\frac{1}{2}, \frac{1}{2})$ leads to a non-zero expectation value for $\langle c^\dagger_{\mathbf{k},\sigma} c_{\mathbf{k}+\mathbf{Q},\sigma} \rangle$ and therefore to a symmetry broken ground state with an anti-ferromagnetic moment. The staggered magnetization is the order parameter of an anti-ferromagnetic state. It counts spins with an alternating sign for each lattice site. It is maximized for a perfect distribution of alternating spins. Using $\mathrm{e}^{\mathbf{Q}\mathbf{R}_i} = (-1)^i$ we can write the expectation value of the staggered magnetization in momentum space,

$$m_s = m_{s,\uparrow} - m_{s,\downarrow}, \tag{3.5}$$

$$\begin{aligned} m_{s,\sigma} &= \frac{1}{N} \sum_i (-1)^i \langle c^\dagger_{i,\sigma} c_{i,\sigma} \\ &= \frac{1}{N} \sum_{\mathbf{k}} \langle c^\dagger_{\mathbf{k},\sigma} c_{\mathbf{k}+\mathbf{Q},\sigma} \rangle. \end{aligned} \tag{3.6}$$

In terms of the above defined parameters equation 3.3 simplifies finally to

$$\hat{H} = \sum_{\mathbf{k},\sigma} \left(\varepsilon_{\mathbf{k}} - \mu + U n_{-\sigma} \right) c^\dagger_{\mathbf{k},\sigma} c_{\mathbf{k},\sigma} + U m_{s,-\sigma} \sum_{\mathbf{k},\sigma} c^\dagger_{\mathbf{k}+\mathbf{Q},\sigma} c_{\mathbf{k},\sigma}. \tag{3.7}$$

We are left with a Hamilton operator consisting only of single particle operators. That shows the idea of the mean field approach, describing non-interacting particles that are exposed to an averaged field. This field is the result off the sum of all particles in the system. It's value will therefore be influenced by the particles itself. As a result we have to solve the equations for the fields self-consistently, which will be done in the next section. The first term in the above mean field Hamiltonian represents the mean repulsion due to the equal charge of the electrons. The strength of the repulsion seen by a particle with a certain spin is proportional to the number density of particles with the opposite spin, since the on-site interaction couples only particles with different spin.

The second term corresponds to the coupling to a staggered magnetic field, that is a magnetic field with an alternating orientation on each site. The field strength is proportional to the magnetization of the ground state and given by Um_s.

Mean Field Propagators

The mean field Hamiltonian gives rise to two different propagators. First we get the diagonal contribution, second an off-diagonal one from the staggered component. The propagators are defined by

$$G_{\mathbf{k}}(\tau) = -\langle \mathcal{T}_\tau c_{\mathbf{k},\sigma}(\tau) c^\dagger_{\mathbf{k},\sigma}(0)\rangle \tag{3.8}$$

$$F_{\mathbf{k}}(\tau) = -\langle \mathcal{T}_\tau c_{\mathbf{k}+\mathbf{Q},\sigma}(\tau) c^\dagger_{\mathbf{k},\sigma}(0)\rangle \tag{3.9}$$

with the imaginary time ordering operator $\mathcal{T}_\tau$, acting on a pair of fermion operators according to

$$\begin{aligned}\mathcal{T}_\tau \hat{A}(\tau_1)\hat{B}(\tau_2) &= -\Theta(\tau_1-\tau_2)\hat{A}(\tau_1)\hat{B}(\tau_2) + \Theta(\tau_2-\tau_1)\hat{B}(\tau_2)\hat{A}(\tau_1) \\ &= \begin{cases} -\hat{A}(\tau_1)\hat{B}(\tau_2) \text{ for } \tau_1 \geq \tau_2 \\ \hat{B}(\tau_2)\hat{A}(\tau_1) \text{ for } \tau_1 < \tau_2 \end{cases}\end{aligned} \tag{3.10}$$

From this definition it follows that n_σ and $m_{s,\sigma}$ can be expressed in terms of propagators, namely through

$$n_\sigma \quad = \frac{1}{N}\sum_{\mathbf{k}} \left(1 - G_{\mathbf{k},-\sigma}(0)\right) \tag{3.11}$$

$$m_{s,\sigma} = -\frac{1}{N}\sum_{\mathbf{k}} F_{\mathbf{k},-\sigma}(0) \tag{3.12}$$

The equation of motion for operators, $\frac{\mathrm{d}}{\mathrm{d}\tau}\hat{A} = [H,\hat{A}] + \frac{\partial}{\partial_\tau}\hat{A}$, determines the dependence of the propagators on imaginary time. Using the definition of propagators in Eq. (3.9) and the equation of motion, we get the differential equation.

$$\begin{aligned}\partial_\tau G_{\mathbf{k},\sigma}(\tau) = \delta(\tau)\langle c_{\mathbf{k},\sigma}(\tau)c^\dagger_{\mathbf{k},\sigma}(0) + c^\dagger_{\mathbf{k},\sigma}(0)c_{\mathbf{k},\sigma}(\tau)\rangle \\ +\Theta(\tau)\langle [\hat{H}, c_{\mathbf{k},\sigma}(\tau)]c^\dagger_{\mathbf{k},\sigma}(0)\rangle \\ -\Theta(-\tau)\langle c^\dagger_{\mathbf{k},\sigma}(0)[\hat{H}, c_{\mathbf{k},\sigma}(\tau)]\rangle\end{aligned} \tag{3.13}$$

Here we used $\partial_\tau\Theta(\tau) = \delta(\tau)$. The commutators can be evaluated using the identity $[AB,C] = A\{B,C\} - \{A,C\}B$ and the anti-commutation rules for the creation and annihilation operators in equation 2.16. This results in

$$[H, c_{\mathbf{k},\sigma}(\tau)] = -\left(\varepsilon_{\mathbf{k}} - \mu + Un_{-\sigma}\right) c_{\mathbf{k},\sigma}(\tau) - Um_{s,-\sigma}c_{\mathbf{k}+\mathbf{Q},\sigma}(\tau) \tag{3.14}$$

Putting this back in equation (3.13) together with the definitions for G and F, we get

$$\begin{aligned}\partial_\tau G_{\mathbf{k},\sigma}(\tau) = \delta(\tau)\langle\{c_{\mathbf{k},\sigma}(\tau), c^\dagger_{\mathbf{k},\sigma}(0)\}\rangle - (\varepsilon_{\mathbf{k}} - \mu + Un_{-\sigma})\, G_{\mathbf{k},\sigma}(\tau) \\ -Um_{s,-\sigma}F_{\mathbf{k},\sigma}(\tau)\end{aligned} \tag{3.15}$$

In the next step we take the Fourier transform of this equation. The Fourier transformed propagator is related to the propagator in imaginary time through

$$G_{\mathbf{k},\sigma}(\tau) = \frac{1}{\beta}\sum_n \mathrm{e}^{-\mathrm{i}\omega_n\tau} G_{\mathbf{k},\sigma}(\mathrm{i}\omega_n) \tag{3.16}$$

$$G_{\mathbf{k},\sigma}(\mathrm{i}\omega_n) = \int_0^\beta \mathrm{d}\tau\, \mathrm{e}^{\mathrm{i}\omega_n\tau} G_{\mathbf{k},\sigma}(\tau) \tag{3.17}$$

The so called fermionic Matsubara frequencies ω_n are given by $\omega_n = \frac{\pi}{\beta}(2n{+}1),\ n \in \mathbb{Z}$. By this definition, the fermionic Greens's functions are anti-periodic with respect to shifts in τ by β, $G(\tau+\beta) = -G(\tau)$. Transforming equation (3.15) to momentum space we get

$$(\mathrm{i}\omega_n - \varepsilon_{\mathbf{k}} + \mu - Un_{-\sigma})\, G_{\mathbf{k},\sigma}(\mathrm{i}\omega_n) = 1 + Um_{s,-\sigma}F_{\mathbf{k},\sigma}(\mathrm{i}\omega_n) \tag{3.18}$$

In the same way, starting from $\frac{\mathrm{d}}{\mathrm{d}\tau}F_{\mathbf{k},\sigma}(\tau)$ we get for the off-diagonal propagator

$$(\mathrm{i}\omega_n - \varepsilon_{\mathbf{k}+\mathbf{Q}} + \mu - Un_{-\sigma})\, F_{\mathbf{k},\sigma}(\mathrm{i}\omega_n) = Um_{s,-\sigma}G_{\mathbf{k},\sigma}(\mathrm{i}\omega_n) \tag{3.19}$$

There is no constant term, since the anti-commutator in 3.15 is zero for off-diagonal momenta. Putting the last two equations together we get the expressions for the propagators

$$\begin{aligned}G_{\mathbf{k},\sigma}(\mathrm{i}\omega_n) &= \frac{(\mathrm{i}\omega_n - \varepsilon_{\mathbf{k}+\mathbf{Q}} + \mu - Un_{-\sigma})}{(\mathrm{i}\omega_n - \varepsilon_{\mathbf{k}+\mathbf{Q}} + \mu - Un_{-\sigma})(\mathrm{i}\omega_n - \varepsilon_{\mathbf{k}} + \mu - Un_{-\sigma}) - U^2m^2_{s,-\sigma}} \\ F_{\mathbf{k},\sigma}(\mathrm{i}\omega_n) &= \frac{Um_{s,-\sigma}}{(\mathrm{i}\omega_n - \varepsilon_{\mathbf{k}+\mathbf{Q}} + \mu - Un_{-\sigma})(\mathrm{i}\omega_n - \varepsilon_{\mathbf{k}} + \mu - Un_{-\sigma}) - U^2m^2_{s,-\sigma}}\end{aligned} \tag{3.20}$$

We can rewrite this in a more appealing way by factorizing the denominator of both propagators. The poles are located at

$$E^\pm_{\mathbf{k},\sigma} = \frac{\varepsilon_{\mathbf{k}} + \varepsilon_{\mathbf{k}+\mathbf{Q}}}{2} - \mu + Un_{-\sigma} \pm \sqrt{\left(\frac{\varepsilon_{\mathbf{k}} - \varepsilon_{\mathbf{k}+\mathbf{Q}}}{2}\right)^2 + U^2m^2_{s,-\sigma}} \tag{3.21}$$

Note that $E^\pm_{\mathbf{k},\sigma} = E^\pm_{\mathbf{k}+\mathbf{Q},\sigma}$, since $\varepsilon_{\mathbf{k}+2\mathbf{Q}} = \varepsilon_{\mathbf{k}}$. These energies correspond to the formation of two bands, defined over the reduced or magnetic Brillouin zone. The antiferromagnetic ordering loweres the symmetry of the crystal, and enlarges

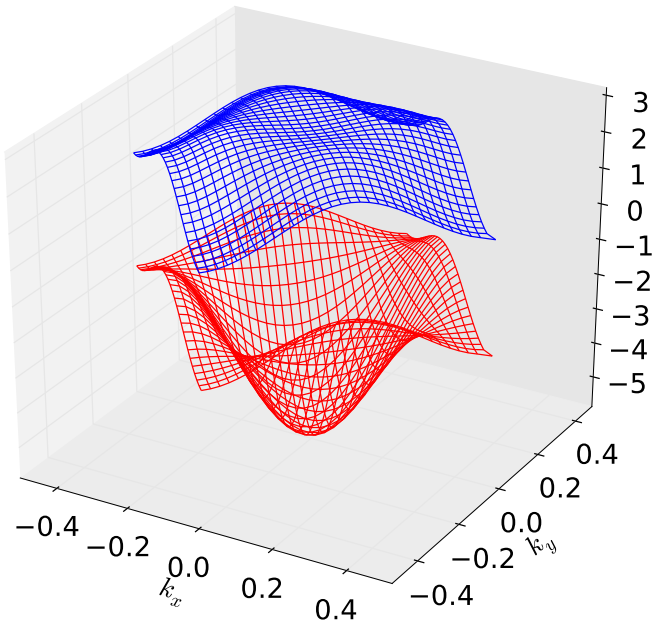

Figure 3.1: $E^+_{\mathbf{k}}$ and $E^-_{\mathbf{k}}$ band for $U = 4.4$ and $(t, t', t'') = (1.0, 0.22, 0.12)$ in dimensionless units.

therfore the unit cell. At the same time the Brillouin zone is reduced, which explains the periodicity in $\mathbf{Q}$. The band structure is shown in figure 3.1. It can be seen clearly, that the bands are well separated. It is conclusive form their expression, that the bands are separated by approximately Um_s for large enough U. The split up is a result of the repulsive interaction and the symmetry breaking of the anti-ferromagnet ground state. The $J = \frac{1}{2}$-band is half filled, the lower of the split bands $E^-_{\mathbf{k}}$ is therefore fully occupied, while $E^+_{\mathbf{k}}$ is remains empty. This makes Sr_2IrO_4 an insulator. This only possible since, because the t_{2g} states were already split into two smaller bands by the strong SOC. Changing the parameters for SOC and electron-electron repulsion a little changes the situation significantly. Sr_2RhO_4, which is equal to Sr_2IrO_4 in structure and electron configuration, just with the $4d$ orbital is metallic[13]. The interaction in the $4d$ orbitals is stronger, while at the same time the SOC is to weak, to create the same bands as in the Ir case. The interaction is then not strong enough, to split the rather broad t_{2g} band. As a result Sr_2RhO_4 is a paramagnetic metal. This shows the importance of strong SOC for the properties of Sr_2IrO_4. It further supports the statement, that Sr_2IrO_4 experiences the effects of both types of mechanisms to create insulators, the charge interaction driven Mott type and the Slater type, which is based on magnetic ordering [3], since its and gap depends on the repulsion as well as the antiferromagnetic ordering.

Using the expressions for the energies $E^{\pm}_{\mathbf{k}}$, the propagators can be expressed in terms of the new bands,

$$G_{\mathbf{k},\sigma}(\mathrm{i}\omega_n) = \frac{\mathrm{i}\omega_n - \varepsilon_{\mathbf{k}+\mathbf{Q}} + \mu - Un_{-\sigma}}{(\mathrm{i}\omega_n - E^+_{\mathbf{k},\sigma})(\mathrm{i}\omega_n - E^-_{\mathbf{k},\sigma})}, \tag{3.22}$$

$$F_{\mathbf{k},\sigma}(\mathrm{i}\omega_n) = \frac{Um_{s,-\sigma}}{(\mathrm{i}\omega_n - E^+_{\mathbf{k},\sigma})(\mathrm{i}\omega_n - E^-_{\mathbf{k},\sigma})}. \tag{3.23}$$

We note that $F_{\mathbf{k},\sigma}$ is invariant under a translation $\mathbf{k} \to \mathbf{k}+\mathbf{Q}$, while $G_{\mathbf{k},\sigma}$ changes depending on the dispersion $\varepsilon_{\mathbf{k}}$.

There is an alternative approach from a diagrammatic point of view, that gives the same differential equation for the propagators. Following the notation of [4], we denote the bare propagator $G^0_{\mathbf{k},\sigma}$ by a single line, the mean field propagators by double lines and the interaction by a dashed line. The off-diagonal propagator $F_{\mathbf{k},\sigma}$ is marked with an doubled arrow head. The diagrams for a self-consistent mean field approximation are shown in figure 3.2.

By including only single loops we neglect again the possibility of quantum fluctuations, i.e. there are no interactions with virtual states. Note that the particles on each site of the interaction have different spins and there is no spin transfer. All straight arrows have therefore the same spin, while the propagators forming the loops have the opposite spin. We reflect the sum up to infinite such interactions by using the mean field propagator after the interaction. Self-consistency is achieved by using the mean field propagators in the loops. This

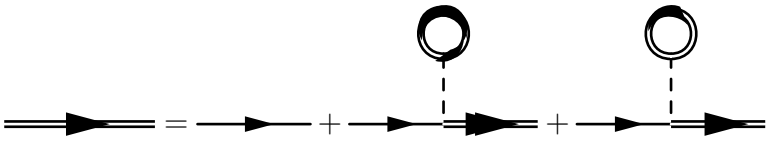

(3.24)

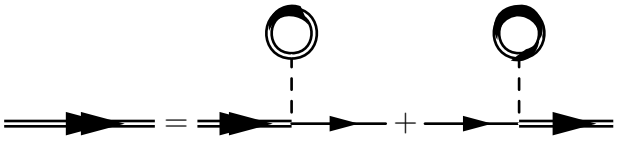

(3.25)

Figure 3.2: Self consistent mean field equations for $G_{\mathbf{k},\sigma}$ and $F_{\mathbf{k},\sigma}$.

reflects the fact, that $m_{s,\sigma}$ and n_σ itself depend on the sum over the respective mean field propagator. As a result we have to solve the equations for $m_{s,\sigma}$ and n_σ iteratively. Inserting the bare propagator $G^0_{\mathbf{k},\sigma}(\mathrm{i}\omega_n) = (\mathrm{i}\omega_n + \varepsilon_{\mathbf{k}} - \mu)^{-1}$ of the non interacting system as well as equations 3.11 and 3.12 reproduces the above expressions for $G_{\mathbf{k},\sigma}$ and $F_{\mathbf{k},\sigma}$.

3.2 Observables

In the chapters above we derived an effective Hamiltonian for the iridates. Furthermore we introduced the Green's functions of the mean field approach. We can use this formalism now, to calculate observable quantities. They can be compared to experiments to validate the calculations. The interaction parameter U has to be fitted to experiments as well.

X-Ray and Neutron Scattering Experiments

The main experimental techniques that resolve the magnetic structure of such materials are inelastic neutron and x-ray scattering experiments. Neutrons are uncharged and do therefore not interact with the charges of atoms and electrons in the crystal. This allows them to penetrate thick probes and to interact well below the surface, which makes measurements of the bulk possible. They interact solely through their intrinsic spin with the crystal, which makes them good candidates for probing the magnetic excitation spectrum.

During the last two decades, resonant inelastic x-ray scattering (RIXS) became an important alternative. It uses high energetic photons, whose energy is tuned to be resonant to an atomic transition in the system. The exited electron is lifted in the bands at the Fermi level, where they can interact with particles close to this band. When the whole created by the incident photon is filled with some electron from that band, a secondary photon is sent out. The secondary photon might have a different energy and momentum due to the dynamics of particles in the relevant band, which is the reason, that this process is inelastic.

In both cases, neutron and photon scattering, we can measure the momentum transfer and energy transfer to the probe. The differential cross section $\frac{\mathrm{d}^2\sigma}{\mathrm{d}\Omega\mathrm{d}\omega}$ is the distribution of secondary particles with a certain momenta. The difference to the momenta of the primary photon is passed to the probe as an excitation. At basic excitations of the system scattering becomes resonant and the differential cross section has a pole. The position $(\mathbf{q}, \omega)$ of these poles reveal therefore the dispersion of magnetic excitations in the material.

The differential cross section is proportional to the imaginary part of the retarded response function [14, Chapter 7.3.1], which will be described in the next paragraph.

$$\frac{\mathrm{d}^2\sigma}{\mathrm{d}\Omega\mathrm{d}\omega} = -2\Im\left(\chi(\omega\mathbf{q})\right) \tag{3.26}$$

Response Functions

Response functions describe the reaction of the system to an external distortion. The distortion is some generalized external force F, for example an electromagnetic field. This force might vary in space and time. It needs to be coupled to the system through some sort of interaction, that is introduced into the Hamiltonian by a additional term $\hat{H}_F = \hat{X}(F)$ for some operator $\hat{X}$. In the simplest case, X is linear in F, that is $X = X'F$. A linear dependence provides a good description for week perturbations of the system, that is for $F \to 0$. X' is then just the first term of an expansion of X. The effect on the system will then be measured by the change in some observable $y = \langle Y \rangle$, which might coincide with the operator X'. The response of the system is then completely encoded in the linear response function χ, which depends in Y and X', but is independent of the external force F.

The dynamic magnetic susceptibility is the linear response function to an external space and time dependent magnetic field $\mathbf{B}(\mathbf{r}, t)$. It couples to the magnetic moment $\mathbf{M}$ in the system through $\int \mathrm{d}^3 r \hat{\mathbf{M}}(\mathbf{r})\mathbf{B}(\mathbf{r}, t)$. The distortion is quantified through $\mathbf{M}$ as well. The magnetic susceptibility is therefore proportional to the expectation value of magnetic structure factor.

$$\chi^{ab}(\mathbf{q}, \omega) = \int \mathrm{d}\tau \mathrm{e}^{\mathrm{i}\omega\tau} \langle M^a(q, \tau) M^b(-\mathbf{q}, 0) \rangle \tag{3.27}$$

Measurements are often performed on a poly-crystals or powder. Therefore we don't have a fixed crystal orientation, but rather an average over all spatial orientations. The effective susceptibility is therefore diagonal with the components

$$\chi_{\text{eff}}^{ab} = \delta^{ab}\text{Tr}(\chi) = \delta^{ab}\langle \mathbf{M}(q,\tau)\mathbf{M}(-\mathbf{q},0)\rangle \tag{3.28}$$

In the simplest case, the spin axes are parallel to the symmetry axes of the crystal. $\mathbf{M}$ is then proportional to the spin $\mathbf{J}$. The spin operator is a one-particle operator with the components $a = x, y, z$, defined as

$$J^a(R_i) = J_i^a = \frac{1}{2}\sum_{\sigma,\sigma'} c_{i,\sigma}^\dagger \left(\sigma^a\right)_{\sigma\sigma'} c_{i,\sigma}, \tag{3.29}$$

σ^a are the Pauli matrices. The momentum space representation is

$$\begin{aligned} J^a(\mathbf{q}) &= \frac{1}{2}\sum_i \sum_{\sigma,\sigma'} \mathrm{e}^{\mathrm{i}\mathbf{q}\mathbf{R}_i} c_{i,\sigma}^\dagger \left(\sigma^a\right)_{\sigma\sigma'} c_i \\ &= \frac{1}{2}\sum_{\mathbf{k}} \sum_{\sigma,\sigma'} c_{\mathbf{k},\sigma}^\dagger \left(\sigma^a\right)_{\sigma\sigma'} c_{\mathbf{k}+\mathbf{q},\sigma'} \end{aligned} \tag{3.30}$$

In Sr_2IrO_4 it is the field of the ligands, that define the spin axes. The octahedra are rotated by $\pm\Theta$ in the x-y-plane in a staggered pattern. It is therefore necessary, to project the spin components on the axes of the lattice at each site. The relation between the magnetic moment, expressed in the axis of thelattice, and the spin $\mathbf{J}_i$ at site i is therefore related by a space dependent coordinate transformation. The transformation matrix at site i is

$$\mathbf{M}_i = \begin{pmatrix} \cos(\Theta) & -(-1)^i\sin(\Theta) & 0 \\ (-1)^i\sin(\Theta) & \cos(\Theta) & 0 \\ 0 & 0 & 1 \end{pmatrix} \mathbf{J}_i \tag{3.31}$$

This transformation can lead to a small ferromagnetic moment in an antiferromagnetic ground state. If we describe the antiferromagnetic ordering with respect to the x-axis of the spins, then we get a net magnetization in y-direction, since the alternating sign in the transformation matrix cancels the spin flip in the antiferromagnetic ordering.

The ferromagnetic moment is proportional to the antiferromagnetic ordering times the projected component,

$$m = \sin\Theta m_s. \tag{3.32}$$

The alternating sign $(-1)^i$ in the rotations express the staggered pattern and can be expressed through the wave vector of antiferromagnetic ordering $\mathbf{Q}$, which

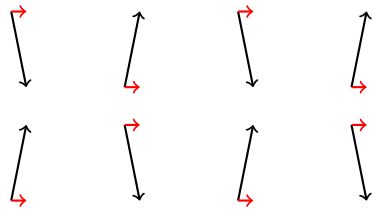

Figure 3.3: The staggered rotation of antiferromagnetic spins lead to a net ferromagnetic moment (red)

reads $(-1)^i = \mathrm{e}^{\mathrm{i}\mathbf{Q}\mathbf{R}_i}$. In momentum space, the relation between magnetic moment and spin is therefore

$$\begin{pmatrix} M^x_{\mathbf{q}} \\ M^y_{\mathbf{q}} \\ M^z_{\mathbf{q}} \end{pmatrix} = -2\mu_b \begin{pmatrix} \cos(\Theta) J^x_{\mathbf{q}} - \sin(\Theta) J^y_{\mathbf{q}+\mathbf{Q}} \\ \cos(\Theta) J^y_{\mathbf{q}} + \sin(\Theta) J^x_{\mathbf{q}+\mathbf{Q}} \\ J^z_{\mathbf{q}} \end{pmatrix} \tag{3.33}$$

We can replace $\mathbf{M}$ in equation 3.28 and get

$$\begin{aligned} \chi_{\text{eff}}(\omega, \mathbf{q}) = &\cos^2\Theta \left(\chi^{xx}_J(\omega, \mathbf{q}) + \chi^{yy}_J(\omega, \mathbf{q})\right) \\ &+ \sin^2\Theta \left(\chi^{xx}_J(\omega, \mathbf{q}+\mathbf{Q}) + \chi^{yy}_J(\omega, \mathbf{p}+\mathbf{Q})\right) + \chi^{zz}_J \end{aligned} \tag{3.34}$$

Where we introduced the spin susceptibility $\chi^{ab}_J(\tau, \mathbf{q} = \langle J^a(\tau, \mathbf{q}) J^b(0, \mathbf{q})\rangle$. Based on the transformation of Pauli matrices $\sigma^{\pm} = \sigma^x \pm \mathrm{i}\sigma^y$ we get the spin components $J^{\pm}$, which fulfil the relation $J^{\pm} = (J^{\mp})^{\dagger}$. Using this relation we can express the sum of xx and yy components of the spin susceptibility in terms of $+-$ and $-+$ components,

$$\chi^{xx}_J + \chi^{yy}_J = \chi^{+-}_J + \chi^{-+}_J = 2\chi^{+-}_J \tag{3.35}$$

The magnetic susceptibility gets therefore the form

$$\chi_{\text{eff}}(\omega, \mathbf{q}) = 2\cos^2\Theta \chi^{+-}_J(\omega, \mathbf{q}) + 2\sin^2\Theta \chi^{+-}_J(\omega, \mathbf{q}+\mathbf{Q}) + \chi^{zz}_J(\omega, \mathbf{q}) \tag{3.36}$$

3.2.1 Dynamic Magnetic Susceptibility In The Green's Function Formalism

We can expand the spin susceptibility in terms of Green's functions. We will first calculate the transverse susceptibility χ^{+-}_J, by summing up the relevant diagrams. The longitudinal component χ^{zz}_J is then calculated in a similar manner.

Expressing χ^{+-}_J and χ^{-+}_J in creation and destruction operators gives

$$\begin{aligned} \chi^{+-}(\mathbf{q}, \omega) &= \int_0^{\beta} \mathrm{d}\tau \mathrm{e}^{\mathrm{i}\omega\tau} \langle \mathcal{T}_\tau S^+(\mathbf{q}, \tau) S^-(-\mathbf{q}, 0)\rangle \\ &= \int_0^{\beta} \mathrm{d}\tau \mathrm{e}^{\mathrm{i}\omega\tau} \sum_{\mathbf{k}\mathbf{k}'} \langle c^{\dagger}_{\mathbf{k},\downarrow}(\tau) c_{\mathbf{k}+\mathbf{q},\uparrow}(\tau) c^{\dagger}_{\mathbf{k}'+\mathbf{q},\downarrow}(0) c_{\mathbf{k}',\uparrow}(0)\rangle. \end{aligned} \tag{3.37}$$

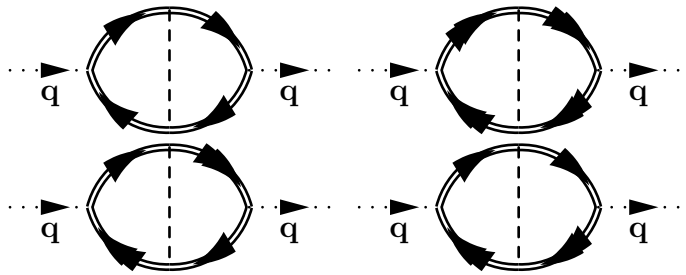

Figure 3.4: some of the first order diagrams contributing to $\chi^{+-}(\mathbf{q}, \mathrm{i}\omega_n)$.

As a four point correlation function, it describes the propagation of a particle-hole pair with momentum $\mathbf{q}$. We restrict the sum over all diagrams to the most relevant subclass. It is given by diagrams, which form a chain of bubbles or a ladder of particle-hole pairs. This approximation is known as the random phase approximation (RPA). Since the particle and hole propagator of such basic excitations are always connected at the same vertices, their product is independent of the phase. This would not be the case if interactions with quantum fluctuations were taken into account. The situation corresponds to a phase that is randomly distributed and cancels therefore in the thermodynamic limit. Those are furthermore the diagrams, where each occurrence of $\frac{U}{N}$ is paired with a sum over momenta, which runs over all N momenta. Diagrams beyond the RPA have fewer integrations over free momenta and are therefore suppressed in the large N limit. The first order bubble diagrams of the RPA expansion are shown in figure 3.4. Each step in the ladder consists a product of two propagators, which can be the diagonal one $G_{\mathbf{q},\sigma}$ or the off-diagonal propagator $F_{\mathbf{q},\sigma}$, as well as the interaction term $\frac{U}{N}$ times a delta function. The building blocks for the ladder diagrams are listed in table 3.1. Momentum conversation at each vertex limits the sum over momenta in each block to $\mathbf{k}' = \mathbf{k} + \mathbf{q}$ or $\mathbf{k}' = \mathbf{k} + \mathbf{q} + \mathbf{Q}$ The second possibility is due to the off-diagonal propagator $F_{\mathbf{k},\sigma}$, that adds $\mathbf{Q}$ to the momentum. Each block consists of a sum over the Brillouin zone, we can therefore shift the momentum in the product of propagators without changing the value of the sum. As mentioned above, only $G_{\mathbf{k},\sigma}$ changes under a shift of $\mathbf{Q}$, $F_{\mathbf{k},\sigma}$ however is invariant under such a transformation. Therefore only x will change it's value for $\mathbf{q} \to \mathbf{q} + \mathbf{Q}$, in all other situations the sum is unchanged, as the transformation can be absorbed in $F_{\mathbf{k},\sigma}$, We will write $\bar{x}$ to denote the expression for x with $\mathbf{k} - \mathbf{k}' = \mathbf{q} + \mathbf{Q}$. When combining the building blocks of the ladder we have to keep track of the momentum difference $\mathbf{k} - \mathbf{k}'$ in the sum over paired propagators. In order to deal with the right momenta between upper and lower propagator we rewrite it as a 2×2 matrix equation and pick the value that corresponds to having $\mathbf{q}$ as the external momentum on both sides of the diagram. The upper component in this matrix equation corresponds to $\mathbf{k} - \mathbf{k}' = \mathbf{q}$, while the lower

λ	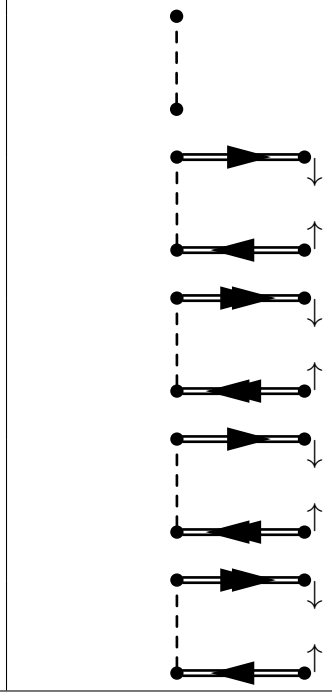	$\frac{U}{N}\delta(\mathbf{k}_1 - \mathbf{k}_2 + \mathbf{k}_3 - \mathbf{k}_4)$
λx		$\frac{U}{N}\sum_{\mathbf{k},n'} G_{\mathbf{k},\downarrow}(\mathrm{i}\omega_{n'})G_{\mathbf{k}+\mathbf{q},\uparrow}(\mathrm{i}\omega_{n'} + \mathrm{i}\omega_n)$
λy		$\frac{U}{N}\sum_{\mathbf{k},n'} F_{\mathbf{k},\downarrow}(\mathrm{i}\omega_{n'})F_{\mathbf{k}+\mathbf{q},\uparrow}(\mathrm{i}\omega_{n'} + \mathrm{i}\omega_n)$
λz_1		$\frac{U}{N}\sum_{\mathbf{k},n'} G_{\mathbf{k},\downarrow}(\mathrm{i}\omega_{n'})F_{\mathbf{k}+\mathbf{q},\uparrow}(\mathrm{i}\omega_{n'} + \mathrm{i}\omega_n)$
λz_2		$\frac{U}{N}\sum_{\mathbf{k},n'} F_{\mathbf{k},\downarrow}(\mathrm{i}\omega_{n'})G_{\mathbf{k}+\mathbf{q},\uparrow}(\mathrm{i}\omega_{n'} + \mathrm{i}\omega_n)$

Table 3.1: building blocks of ladder diagrams for $\chi^{+-}(\mathbf{q}, \mathrm{i}\omega_n)$

one corresponds to $\mathbf{k} - \mathbf{k}' = \mathbf{q} + \mathbf{Q}$. The full equation reads then

$$\chi_J^{+-}(\mathbf{q}, \mathrm{i}\omega_n) = \begin{pmatrix} x + y & z_1 + z_2 \end{pmatrix} \cdot \sum_{m=0}^{\infty} (-\lambda \mathbf{M})^m \cdot \begin{pmatrix} -1 \\ 0 \end{pmatrix} \tag{3.38}$$

with the matrix $\mathbf{M}$ combining all the possibilities for one new step in the ladder for each order m,

$$\mathbf{M} = \begin{pmatrix} x + y & z_1 + z_2 \\ z_1 + z_2 & \bar{x} + y \end{pmatrix} \tag{3.39}$$

At the end of a ladder diagram however we have to fulfil $\mathbf{k} - \mathbf{k}' = \mathbf{q}$. The last vector ensures the right external momentum at the end and takes care of the minus sign, arising from the loop. The infinite sum of bubble diagrams represents a geometric series and has an analytical expression. Using the expression for geometric sums for matrices we can express the infinite sum through

$$\sum_{m=0}^{\infty} (-\lambda \mathbf{M})^m = (\mathbf{1} + \lambda \mathbf{M})^{-1} \tag{3.40}$$

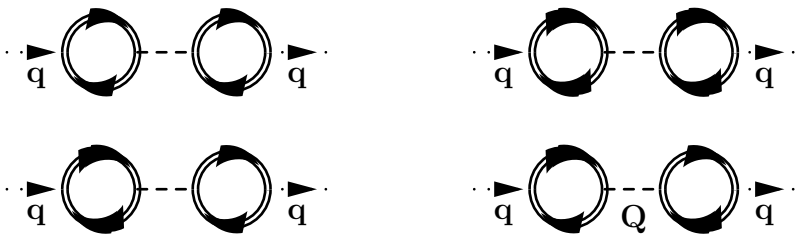

Figure 3.5: some of the first order diagrams contributing to χ^{zz}.

The whole expression reads then

$$\chi^{+-}_{\mathrm{RPA}}(\mathbf{q}, \mathrm{i}\omega_n) = \frac{-(x+y)\,(1+\lambda(\bar{x}+y)) + \lambda(z_1+z_2)^2}{(1+\lambda(x+y))\,(1+\lambda(\bar{x}+y)) - \lambda^2(z_1+z_2)^2} \tag{3.41}$$

In order to deal with the infinite Matsubara frequency summation we use the procedure from Appendix A, as we did for finding m_s. The remaining expression depends then only on $\mathrm{i}\omega_n$. We are interested in the dependence on real frequencies ω. Expression 3.41 possesses poles on the real axis, making a simple replacement of $\mathrm{i}\omega_n$ with $\omega \in \mathbb{R}$ impossible. We perform the analytical continuation $\mathrm{i}\omega_n \to \omega + \mathrm{i}\eta$ with $\omega, \eta \in \mathbb{R}$ and for a small $\eta > 0$. By choosing η to be positive we get the retarded response function. The expression can then be evaluated by carrying out the sum over the momenta using a small numerical value for η. This allows us not only to calculate the imaginary part, a finite value of η smoothes the resulting response function. In general, for a function of the type $(\omega + \mathrm{i}\eta - E)^{-1}$, the imaginary part is $\frac{-\eta}{\eta^2+(\omega-E)^2} \overset{\eta\to 0}{\longrightarrow} \pi\delta(\omega - E)$. In the actual limit of vanishing η we expect a delta function, whose poles might not match the discretized momenta of the grid exactly. Broadening the delta function ensures to not miss momenta due to a finite sized grid and yields a result closer to actual measurements, where the response function also shows a finite line width.

The position of the poles finally yields the spin-wave dispersion $\omega(\mathbf{q})$. Furthermore, we expect a continuum at higher energies.

Longitudinal Magnetic Susceptibility

The longitudinal spin susceptibility consists of particle-hole propagators with equal spin. This doesn't allow for interactions between particle and hole, but for recombination and creation of a new pair. The diagrams to be summed are therefore chains of bubbles. Some exampled of the first order terms contributing to χ^{zz}_J are shown in figure 3.5. Two consecutive bubbles must have opposite spin, so they can be connected by the interaction term.

The bubbles in table 3.2 show the building blocks of the chains, that are summed up in the diagrammatic expansion of χ^{zz}_J in the random phase approximation. The second column shows the relation to the previously defined products

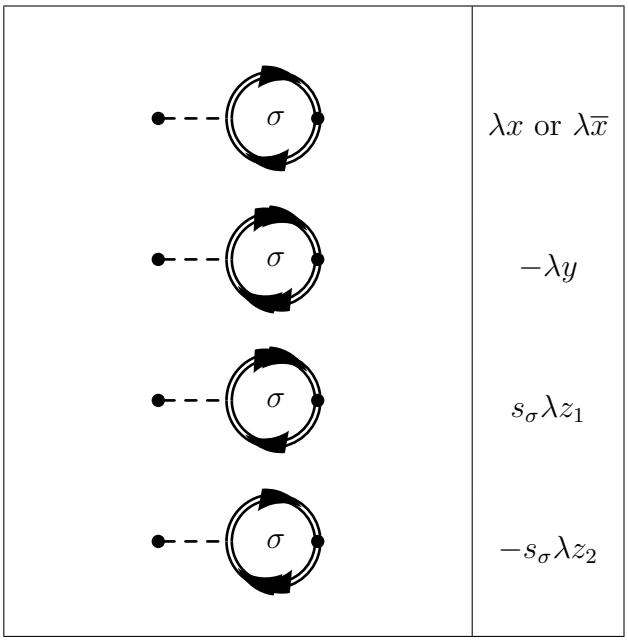

Table 3.2: elements of the chain in χ_J^{zz}

of operators x, y, z_1, z_2. Since only $F_{\mathbf{k},\sigma}$ depends on the spin with the simple relation $F_{\mathbf{k},-\sigma} = -F_{\mathbf{k},\sigma}$, the relation to the expressions found earlier is just a spin dependent sign. Since the Hubbard interaction couples only spins with opposite orientation, two consecutive bubbles in the row must have opposite spin. The last to blocks, proportional to $s_\sigma z_i$ change the momentum, that is transferred through the interaction by $\mathbf{Q}$. The difference of $\mathbf{k}$ and $\mathbf{k}'$ between the upper and lower propagator in the bubble is therefore restricted to the external momentum $\mathbf{q}$ and a shifted momentum, $\mathbf{q} + \mathbf{Q}$. In order to keep track of the alternating spins and the right transferred momentum, we set up a matrix as before. This time we have to deal with four components, that is spin and transferred vector. Let the components be $((\mathbf{q},\uparrow),(\mathbf{q}+\mathbf{Q},\uparrow),(\mathbf{q},\downarrow),(\mathbf{q}+\mathbf{Q},\downarrow))^T$. The sum over all possible chains can then be expressed as

$$\begin{aligned}\chi_J^{zz} &= \langle \sum_{\mathbf{k}\mathbf{k}'} (c^\dagger_{\mathbf{k},\uparrow} c_{\mathbf{k}+\mathbf{q},\uparrow} - c^\dagger_{\mathbf{k},\downarrow} c_{\mathbf{k}+\mathbf{q},\downarrow})(c^\dagger_{\mathbf{k}',\uparrow} c_{\mathbf{k}'+\mathbf{q},\uparrow} - c^\dagger_{\mathbf{k}',\downarrow} c_{\mathbf{k}'+\mathbf{q},\downarrow}) \rangle \\ &= \begin{pmatrix} x-y \\ z_1 - z_2 \\ y - x \\ z_1 - z_2 \end{pmatrix}^T \sum_{n=0}^{\infty} (-\lambda)^n \begin{pmatrix} 0 & \mathbf{M}_\downarrow \\ \mathbf{M}_\uparrow & 0 \end{pmatrix}^n \begin{pmatrix} 1 \\ 0 \\ -1 \\ 0 \end{pmatrix} \end{aligned} \tag{3.42}$$

The last vector ensures again that we pick the bubbles with $\mathbf{k} - \mathbf{k}' = \mathbf{q}$ at the end of the chain. The matrix $\mathbf{M}_\sigma$ is defined similar to $\mathbf{M}$ of equation 3.39. It

differs only by the sign changes of it entries,

$$\mathbf{M}_\sigma = \begin{pmatrix} x-y & s_\sigma(z_1-z_2) \\ s_\sigma(z_1-z_2) & \overline{x}-y \end{pmatrix} \tag{3.43}$$

The geometric sum can be regrouped in terms of even and odd powers of n. After taking out one power from the odd sum we can add the two sums again and multiply it with unity plus on times the original matrix,

$$\begin{aligned} \sum_n \lambda^n \begin{pmatrix} 0 & \mathbf{M}_\downarrow \\ \mathbf{M}_\uparrow & 0 \end{pmatrix}^n &= \sum_n \lambda^{2n} \begin{pmatrix} \mathbf{M}_\downarrow\mathbf{M}_\uparrow & 0 \\ 0 & \mathbf{M}_\uparrow\mathbf{M}_\downarrow \end{pmatrix}^{2n} \begin{pmatrix} 1 & -\lambda\mathbf{M}_\uparrow \\ \lambda-\mathbf{M}_\downarrow & 1 \end{pmatrix} \\ &= \begin{pmatrix} (1-\lambda^2\mathbf{M}_\downarrow\mathbf{M}_\uparrow)^{-1} & 0 \\ 0 & (1-\lambda^2\mathbf{M}_\uparrow\mathbf{M}_\downarrow)^{-1} \end{pmatrix} \begin{pmatrix} 1 & -\lambda\mathbf{M}_\uparrow \\ -\lambda\mathbf{M}_\downarrow & 1 \end{pmatrix} \end{aligned} \tag{3.44}$$

Inserting the definition of $\mathbf{M}_\sigma$ in equation 3.42 and writing it out yields the closed form expression for χ_J^{zz} in the random phase approximation,

$$\begin{aligned} \chi_J^{zz} = 2\Big(&-(1-\lambda^2(\overline{x}-y)^2+\lambda^2(z_1-z_2)^2)(x-y)(1+\lambda(x-y)) \\ &+(1-\lambda^2(x-y)^2+\lambda^2(z_1-z_2)^2)\lambda(z_1-z_2) \\ &+\lambda^2(x-\overline{x})(z_1-z_2)^2(1+2\lambda(x-y))\Big) \\ &\times(\det(1-\mathbf{M}_\uparrow\mathbf{M}_\downarrow))^{-1} \end{aligned} \tag{3.45}$$

with the denominator

$$\begin{aligned} \det(1-\mathbf{M}_\uparrow\mathbf{M}_\downarrow) = \big((1-\lambda^2(x-y)^2+\lambda^2(z_1-z_2)^2\big) \\ \cdot\big(1-\lambda^2(\overline{x}-y)^2+\lambda^2(z_1-z_2)^2\big) \\ +\lambda^4(z_1-z_2)^2(x-\overline{x})^2 \end{aligned} \tag{3.46}$$

The expressions for χ_J^{+-} and χ_J^{zz} are imaginary through the use of imaginary frequencies in x, y, z_1 and z_2. We want to evaluate the expressions for real frequencies, but we have to keep an infinitesimal imaginary part due to poles on the real frequency axis. This leads to a vanishing imaginary part, except for a vanishing denominator, where it resembles a delta function. In order to find the poles it is therefore sufficient to evaluate the denominator to 0.

3.2.2 Corrections due to Quantum Fluctuations

The simplifications we made in order to treat the Hubbard model in the mean field approach, eliminate any effects that are caused by quantum fluctuations. These

effects may be small and we are able to cover the main features of the system with our simplified description, but their effect have to be taken into account, especially when comparing calculations to measurements, where absolute values of observables are relevant. One example is the staggered magnetization, that is overestimated in the mean field treatment. Fluctuations around the antiferromagnetic ground state act as a distortion to the ordering and lower therefore the expectation value of m_s.

Calculating the full corrections is beyond the scope of this thesis, but we can account for some major corrections, that have no complicated dependencies. For the Heisenberg model, the corrections to the spin-wave-velocity, denoted by $\mathcal{Z}_c$, are well known. They are given by the higher order terms of the $\frac{1}{S}$ expansion. The main contribution is independent of momentum and frequency. Higher order terms are an order of magnitude smaller and their momentum dependence changes the correction factor by 2% at max. Usually one uses therefore a constant of $\mathcal{Z}_c = 1.18$ value to renormalize the whole spin-wave dispersion [15].

We will see that our calculation scheme provides the result of linear spin-wave theory without further corrections in the limit of large U. The Hubbard model can be expanded in this limit. The correction factor is the same as in the Heisenberg model, as one would except. In reference [16], Singh calculated corrections in the Hubbard model, given by diagrams corresponding to quantum fluctuations, and found a value consistent with $\mathcal{Z}_c$. We asume that the correction does not change substantially for smaller U and correct ω in the expression for the dynamic magnetic susceptibility by the constant $\mathcal{Z}_c = 1.18$.

Chapter 4

Results

4.1 Specifications

For all calculations we use dimensionless quantities. Firstly, we set the lattice spacing to unity, $a = 1$. The resulting momenta are therefore given by $(\frac{2\pi n}{N}, \frac{2\pi m}{N})$ for $n, m \in [-\frac{N}{2}, \frac{N}{2})$. Furthermore, we express all energy in units of t, reducing the number of free parameters in the Hamiltonian therfore by one. It depends now on only on the parameters ${}^{U}/_{t}$, ${}^{\mu}/_{t}$ and eventually ${}^{t'}/_{t}$ and ${}^{t''}/_{t}$. Temperatures are scaled accordingly with $k_b = 1$. If not otherwise specified, we use only dimensionless units from now on and we will drop ${}^{\cdot}/_{t}$ and write just the corresponding symbol, assuming it is in units of t.

Since the Hubbard model reduces electron-electron interactions in a very crude manner by taking only on-site interactions into account, its only free parameter U is treated as an adjustable parameter, without an external reference value from other calculations or measurements. For this reason the Hubbard model cannot be seen as a first-principle method [12], but rather an effective model, that extends a first principle method – the band structure – by introducing one adjustable parameter. The value of U in materials is not directly observable, but relates to physical quantities as for example the gap in the electrical excitation spectrum. There are other methods using a Hubbard-like interaction, such as LDA+SO+U calculations. The U we found can then be compared to the one found through this methods. Furthermore it allows us to compare the strength of interaction effects in similar materials in relation to each other.

Numerical calculations were performed in two dimensions due to the layered structure of Sr_2IrO_4, using a grid of size 256×256. As a direct result from the discrete Fourier transformation, we get discrete momenta in the Brillouin zone. The sum over momenta in Greens functions is therefore restricted to 256×256 values. The magnetic susceptibility $\chi(\mathbf{q}, \omega)$ was calculated for different values of $\mathbf{q}$. We choose a path along the symmetry lines of the Brillouin zone, that covers the most interesting features of the dispersion. Due to symmetry in the band

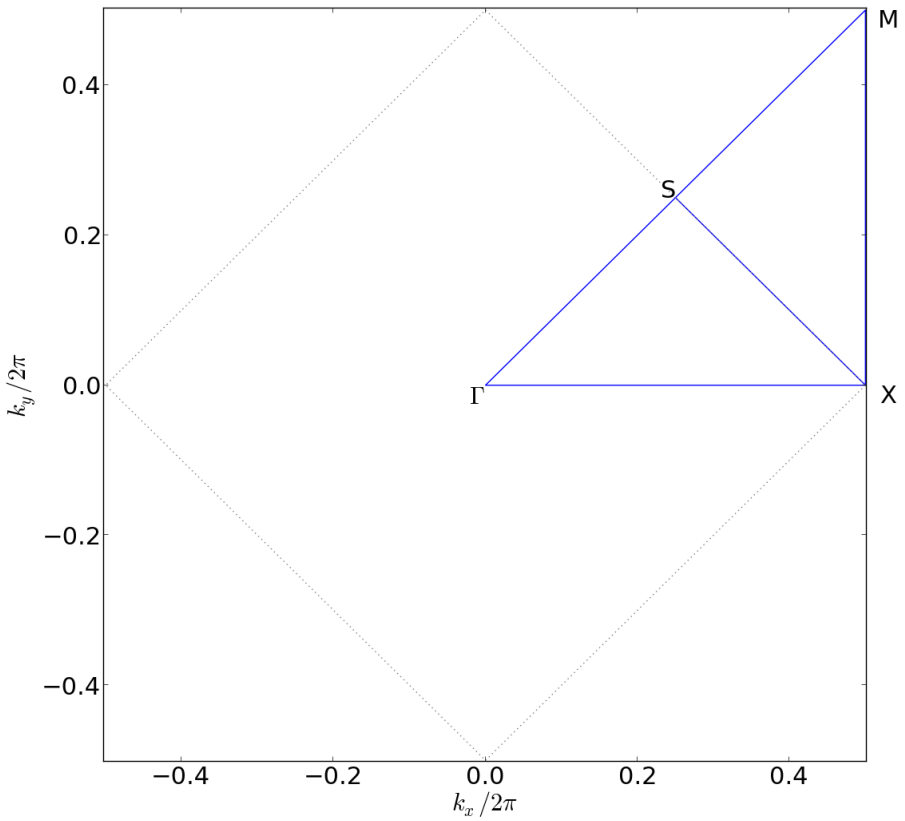

Figure 4.1: path through the Brillouin zone (blue), connecting S-X-M-S-Γ-X. The grey dotted line is the boundary of the magnetic Brillouin zone.

structure energies $\varepsilon_{\mathbf{k}}$ and therefore in the energies $E^{\pm}_{\mathbf{k}}$ as well, it is sufficient to restrict oneself to just a quarter of the Brillouin zone. The most basic dependence on $\mathbf{q}$ is through a cosine, $\cos(q_i)$ or $\cos(2q_i)$, that is independent of the sign of the components q_i. The path chosen for analysis of χ is a standard way of presenting calculations and measurements and makes it easy to compare our results to related work. It covers four directions, which can be parametrized by t ranging from 0 to 1. First the border of the magnetic Brillouin zone perpendicular to the diagonal, $(\frac{1}{4}(2-t), \frac{1}{4}t$, then the k_y-direction along the border of the Brillouin zone, $(0, \frac{1}{2}t)$, the diagonal $(\frac{1}{2}t, \frac{1}{2}t)$ and finally the k_x-direction $(\frac{1}{2}t, 0)$ along the k_y-direction. The path is shown in figure 4.1, together with the boundary of the reduced Brillouin zone. It connects the points $\Gamma = (0,0)$, M=$(\frac{1}{2}, \frac{1}{2})$, S= $(\frac{1}{4}, \frac{1}{4})$ and X=$(\frac{1}{2}, 0)$ in the order S-X-M-S-Γ-X.

The temperature was set to $T = 0.0033$, corresponding to 10K at t=0.258eV.

This is a temperature typically encountered in low-temperature experiments and was used in the measurements that provide our reference data. The Néel temperature for Sr_2IrO_4 is at about 250K[7]. Being far below the Néel temperature is necessary for our assumption of an anti-ferromagnetic ground state. A low temperature is also needed in order to be able to describe the material with an one-band Hubbard model. Comparison of calculations over a wide range of temperatures up to 200K showed no significant dependence on the temperature except for the broadness of peaks.

In the calculation of the magnetic susceptibility χ we need to shift the frequencies infinitesimally above the real axis, in order to get a retarded response function. The small imaginary part of the frequencies are responsible for the imaginary part of χ, which we then relate to the differential cross section. In the calculations we used complex frequencies $\omega^+ = \omega + i\eta$ with a non-zero but small imaginary part η. Choosing a non-infinitesimal value however smears out the delta function, that arises in the limit $\eta \to 0$ in the imaginary part. This can be used to compensate for discretisation effects due to the finite sized grid, because we get a contribution even if the delta function doesn't match one of the discretised momentum. The value has no physical meaning. It changes the broadness and height of the poles. It was chosen as small as possible, but big enough to ensure a smooth result for the response function with pronounced features. Choosing this value to big would wash out the characteristic of the response function, making it hard to analyse. The frequency dependency of propagators and Greens functions is mostly given by $(\omega^+ - E^{\pm}_{\mathbf{k}})^{-1}$ and combinations thereof. As a good starting point we can therefore take the maximum difference in the energies $E^{\pm}$ between to nearby points in the finite sized grid of momenta. For our simplest dispersion, this occurs for example between the momenta $\mathbf{k}_1 = (\pm\frac{1}{4}, \pm\frac{1}{4})$ and $\mathbf{k}_2 = \mathbf{k}_1 + (\frac{1}{\sqrt{N}}, 0)$. As an estimation we can take $U = 4$ and $m = 0.3$ at half filling as a set of typical values, see the discussion below. We get $|E^{\pm}_{\mathbf{k}_1} - E^{\pm}_{\mathbf{k}_2}| = 0.001$ for momenta on a 256×256 grid. Finally, we found $\eta = 0.005$ to be an optimal value. This value is of order 10^{-3} compared to the maximum $\omega(\mathbf{q})$ encountered for typical values of U used in this thesis.

In order to extract the spin wave dispersion, we calculated the imaginary part and plotted it as a colour map over $\mathbf{q}$ and ω. The colour scale is dominated by the highest peaks of χ. In order to visualize the whole dispersion we had to choose a cut off for the highest values. The value was set individually for each calculation such, that it reveals the whole spectrum of possible excitations, but such, that the position of the peaks are well defined. Areas that were set to the maximal value appear therefore slightly broader in the plot. The broadness of the peaks in general is much smaller than in the measurements we compared it to.

4.2 Staggered Magnetization At Half-Filling

We need to fix the parameters n_σ and $m_{s,\sigma}$ of the propagators. They can be expressed through a sum of propagators itself, as shown in equations 3.11 and 3.12. This results in a system of four non-linear coupled equations. At half filling with $\uparrow$-$\downarrow$-symmetry, they can be decoupled and therby be solved in a easier way.

The number density is controlled by the chemical potential, which is another free parameter of the system. The effective spin-$\frac{1}{2}$ states in Sr_2IrO_4 are half-filled, that is $n = 1$. Because of the symmetry between up and down spins we have furthermore $n_\uparrow = n_\downarrow = \frac{1}{2}$ This symmetry is not broken but rather assured by the anti-ferromagnetic ground state.

Due to particle-hole symmetry, the Hamiltonian should be invariant under the replacement $c_{\mathbf{k},\sigma} \leftrightarrow c^\dagger_{\mathbf{k},\sigma}$ In doing this replacement and using the anti-commutation relations for creation and annihilation operators, the Hamilton operator in momentum space reads

$$\begin{aligned}\hat{H} = &\sum_{\mathbf{k},\sigma}(-\varepsilon_{\mathbf{k}} + \mu)c^\dagger_{\mathbf{k},\sigma}c_{\mathbf{k},\sigma} + \frac{U}{N}\sum_{\mathbf{k},\mathbf{k}',\mathbf{q}} c^\dagger_{\mathbf{k},\uparrow}c_{\mathbf{k}-\mathbf{q},\uparrow}c_{\mathbf{k}',\downarrow}c_{\mathbf{k}'+\mathbf{q},\downarrow} \\ &-U\sum_{\mathbf{k}}\left(c^\dagger_{\mathbf{k},\uparrow}c_{\mathbf{k},\uparrow} + c^\dagger_{\mathbf{k},\downarrow}c_{\mathbf{k},\downarrow}\right) + \sum_{\mathbf{k}}(2\varepsilon_{\mathbf{k}} + 2\mu + U)\end{aligned} \tag{4.1}$$

The energy dispersion for holes is given by $\varepsilon^{\text{holes}}_{\mathbf{k}} = -\varepsilon_{\mathbf{k}}$ and by this replacement we get back the original Hamiltonian for particles plus a constant, that does not change our system. We can collect terms proportional to the total number of holes or particles, $nN = \sum_{\mathbf{k},\sigma} c^\dagger_{\mathbf{k},\sigma}c_{\mathbf{k},\sigma}$. The pre-factor of this terms corresponds to the chemical potential for holes. At half-filling it should be the same as for particles, we find therefore

$$\mu = U - \mu \quad \Rightarrow \quad \mu = \frac{U}{2}. \tag{4.2}$$

This allows us to insert $\mu = \frac{U}{2}$ and $n_\sigma = \frac{1}{2}$ immediately in the half filled case.

We furthermore assume that $m_{s,\uparrow} = -m_{s,\downarrow}$. The staggered magnetization may thus be expressed by $m_s = 2\sigma \cdot m_{s,\sigma}$. This relation holds in a perfect anti-ferromagnetic state with at most one particle per site. Double occupied states on the other hand yield contribution to $m_{s,\sigma}$, that is symmetric under for $\uparrow\leftrightarrow\downarrow$ in contrast to the otherwise asymmetric behaviour. The expression for $m_{s,\sigma}$ adds $(-1)^i$ whenever a particle with spin σ is present at site i. This is not affected by the simultaneous presence of a particle with spin $-\sigma$, which will only be seen by $m_{s,-\sigma}$ and will be weighted with the same factor of $(-1)^i$. However, double occupancies can be expected to be distributed evenly throughout the system and we might find as many on the sub-lattice with negative pre-factor as on the positive on. For large systems we can therefore expect this contributions

to vanish in the average over all sites. This restores the antisymmetric relation between $m_{s,\uparrow}$ and $m_{s,\downarrow}$.

As a direct result, $F_{\mathbf{k},\sigma}$ depends only by an overall sign on σ, while the value of $G_{\mathbf{k},\sigma}$ becomes spin independent,

$$G_{\mathbf{k},\uparrow} = G_{\mathbf{k},\downarrow} \qquad F_{\mathbf{k},\uparrow} = -F_{\mathbf{k},\downarrow}. \tag{4.3}$$

In order to calculate $m_{s,\sigma}$ we solve equation 3.12, where we can replace $m_{s,\uparrow}$ by $-m_{s,\downarrow}$, as stated above. We furthermore drop the spin labels on $E^{\pm}_{\mathbf{p},\sigma}$, since they depend only on the absolute value of m_σ and furthermore is $n_\uparrow = n_\downarrow$ as explained above. This decouples the two equations with respect to the spin label. By using the definition of the off-diagonal propagator $F_{\sigma,\mathbf{p}}$ we end up with

$$m_{s,\sigma} = \frac{1}{N} \sum_{\mathbf{p}} \sum_{n \in \mathbb{Z}} \frac{U m_{s,\sigma}}{(\mathrm{i}\omega_n - E^{+}_{\mathbf{p}})(\mathrm{i}\omega_n - E_{\mathbf{p}})} \tag{4.4}$$

The $m_{s,\sigma}$ on the LHS cancels the one in the RHS, but $E^{\pm}$ is still dependent on $|m_{s,\sigma}|$. To deal with the summation over the Matsubara frequencies $\mathrm{i}\omega_n$, we use Cauchy's integral theorem as described in A. The resulting equation

$$1 = \frac{U}{N} \sum_{\mathbf{p}} \frac{1}{E^{+}_{\mathbf{p}} - E^{-}_{\mathbf{p}}} \left(\frac{1}{1 + \mathrm{e}^{\beta E^{+}_{\mathbf{p}}}} - \frac{1}{1 + \mathrm{e}^{\beta E^{-}_{\mathbf{p}}}} \right) \tag{4.5}$$

is solved using the Newton-Raphson method. Figure 4.2 shows an example of the behaviour of m_s for different values of U. The dispersion in this calculation is based on nearest neighbour hopping only, that is $t' = t'' = 0$ on a two-dimensional square lattice. Introducing non-zero t' and t'' showed the same dependency. In the limit of infinite U we get $m_s = 1$, corresponding to a fully anti-ferromagnetic ground state. The strong repulsive interaction prevents double occupancies, because each of them adds U to the energy of the ground state. We will find therefore at max one particle at each site. Half filling requieres then that there is actually a particle at each site. At the same time there are virtual hopping processes to the states of higher energy, which create a possibility to further lower the ground state energy. Virtual hopping between neighbouring sites is only possible if they are occupied by particles with opposite spin. Otherwise it would be forbidden by the Pauli principle, which holds for virtual processes as well. Therefore, an anti-ferromagnetic ground state is energetically preferable to a ferromagnetic one.

Lowering U yields a lower staggered magnetization, since the energy cost for double occupancy gets lower and might be out-weighted by the reduce in kinetic energy due to hopping. At some point we will encounter a transition to an unordered metallic ground state with $m_s = 0$. The closing of the Hubbard gap leads to the transition from the insulating state to a conducting one. The critical

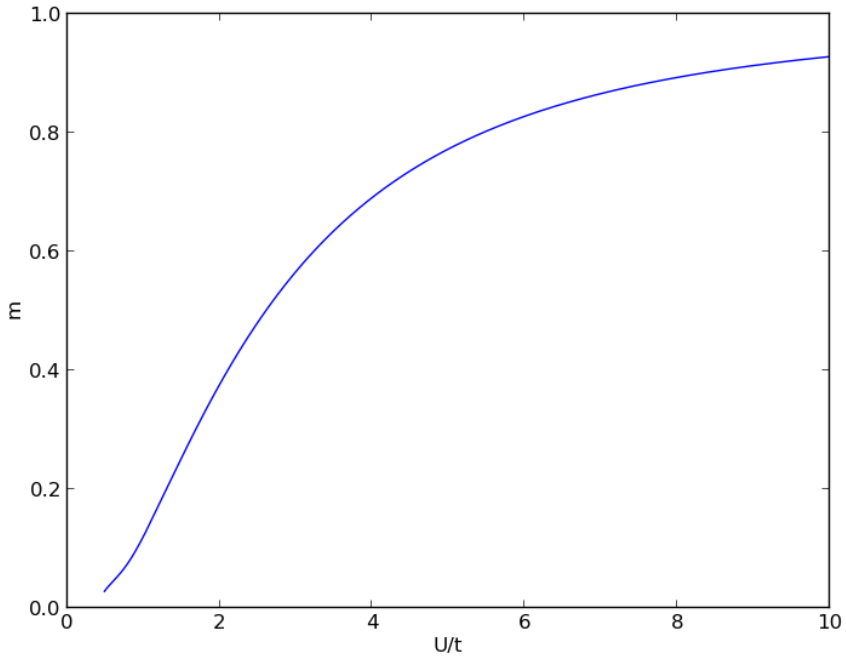

Figure 4.2: staggered magnetization as function of $\frac{U}{t}$

value for this transition is sensitive to the parameters for second- and third-neighbour hopping, even though the dependence of m_s on U above the critical value of U is identical for non-zero and vanishing t' and t''. The critical value was reported by Carter et al. [17] to be in the range $U_c \approx 0.7 - 2.2$, depending of the precise set of parameters. For lower values of U, our assumption of a Hubbard gap and an anti-ferromagnetic ground state is not valid any more and our description is not capable of describing the physical situation any longer. The iterative procedure for m_s is not converging in this situation any longer due to the high sensitivity on the band gap through the factor $(E^p_{\mathbf{k}} - E^-_{\mathbf{k}})^{-1}$. This term is proportional to $\frac{1}{Um_s}$ for momenta with $\varepsilon_{\mathbf{k}} - \varepsilon_{\mathbf{k}+\mathbf{Q}} = 0$. This is exactly the condition for nesting with nesting vector $\mathbf{Q}$, which is present at least at some points. Calculations down to $U = 0.5$ show that the staggered magnetization falls off very fast for low U. The term $(E^+_{\mathbf{k}} - E^-_{\mathbf{k}})^{-1}$ diverges in this case and the iteration procedure becomes numerically unstable. The limitation for this calculation appears therefore for numerical reasons, that become dominant at roughly the value of the transition to the unordered state.

After calculating m_s, the expression for n_σ in terms of the propagator $G_{\mathbf{k},\sigma}$ has also been evaluated and found to be consistent with the above condition for the chemical potential at half-filling.

4.3 Large U Limit

A large U drives the system in an anti-ferromagnet ground state as mentioned above. Hopping at half-filling leads to double occupancies, which are suppressed due to the high energetic cost of U. The spins will therefore be evenly distributed at half filling and the system can be described as an Heisenberg anti-ferromagnet in this limit. By projecting out states with double occupancies we arrive at the Heisenberg model. By downfolding the Hamiltonian to the subspace of only single occupied sites, couplings between sites arise, which can be expanded in orders of $t(\frac{t}{U})^n$. These terms can then be interpreted as hopping processes over multiple sites, resulting in the Heisenberg exchange interaction. The Heisenberg Hamiltonian with only nearest neighbour coupling is

$$\hat{H} = J \sum_{\langle i,j \rangle} \mathbf{S}_i \cdot \mathbf{S}_j, \tag{4.6}$$

which will be an anti-ferromagnetic coupling for positive J, as in this case.

We will expand the expression for χ in terms of $\frac{t^2}{U}$ and compare the resulting dispersion with the linear spin-wave dispersion gained from a $\frac{1}{S}$ expansion of the Heisenberg model. Since we are only interested in the position of the poles in χ, it is sufficient to expand the denominator of equation 3.41 and to solve for its roots,

$$(1 + \lambda(x + y))\,(1 + \lambda(\bar{x} + y)) - \lambda^2 (z_1 + z_2)^2 = 0 \tag{4.7}$$

We note first that the term λy is dominant in this limit, since $\lambda y \sim 1$, while $\lambda x \sim \frac{1}{U^2}$ and $\lambda z_i \sim \frac{1}{U}$ for infinite U. Expanding λy up to first order in $\frac{t^2}{U}$ results in the dispersion

$$\omega(\mathbf{q}) = \frac{4t^2}{U m_s} \sqrt{4 - (\cos q_x + \cos q_y)^2}. \tag{4.8}$$

This is exactly the spin wave dispersion one gets for linear spin waves in a Heisenberg antiferromagnet, with the coupling $J = \frac{4t^2}{U m_s}$. Deriving the Heisenberg model from the Hubbard model yields $J = \frac{4t^2}{U}$ in the first order expansion, which gives a spin wave dispersion that differs by a factor of $\frac{1}{m_s}$ from our result. The dependence of m_s on U shows, that we get a perfect antiferromagnet with $m_s = 1$ for large U, such that the two couplings will be identical in the case, where this approximations are valid.

Linear spin waves are the first term in an $\frac{1}{S}$ expansion of the dispersion in a Heisenberg antiferromagnet. Higher orders renormalize the spin wave dispersion by allowing for quantum fluctuations. It was claimed by Peres et al. that the staggered magnetization in the expression for ω in equation 4.8 plays the role of this renormalization factor [4]. Quantum fluctuations do lower the value of m_s, but in the mean field scheme it tends to 1 for large $\frac{U}{t}$ and is unable to provide such corrections in the case of large U.

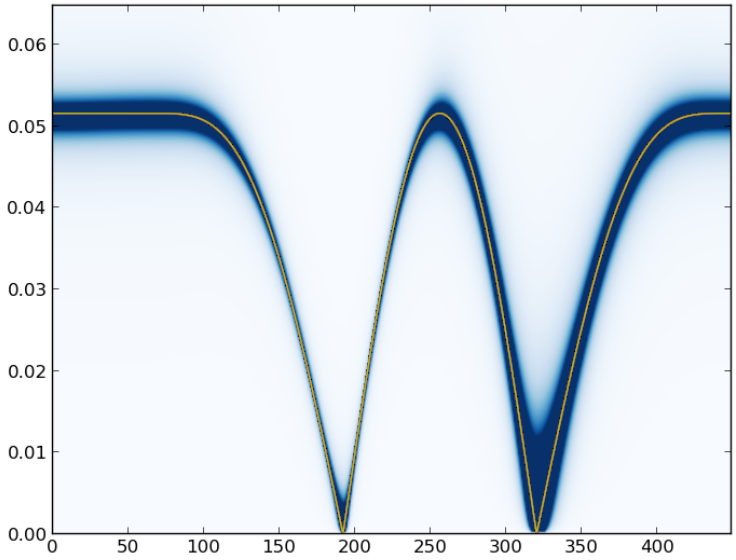

Figure 4.3: spin wave dispersion for $U = 40$ with linear spin-wave theory as comparison

The expression for $\omega(\mathbf{q})$ tells us imediatly, that we get a constant dispersion along the boundary of the magnetic Brillouin zone, $\omega(\frac{1}{2}(1-t), \frac{1}{2}t) = \text{const.}$ for $t \in [0, 1]$.

By using a large value for U in our calculations, we get results that agree well with the unrenormalized case. An example for $U = 40$ can be seen in figure 4.3, together with dispersion for linear spin waves according to equation (4.8).

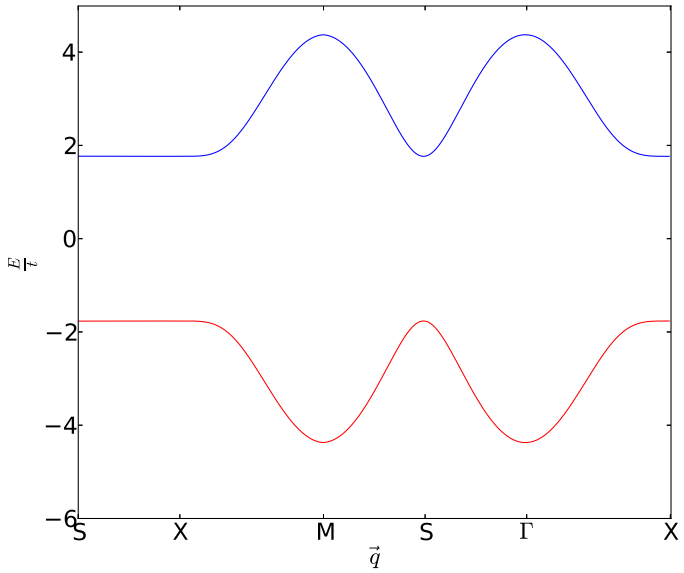

Figure 4.4: $E^{\pm}_{\mathbf{q}}$ for the t-U-model with $U = 4.7t$. $\mathbf{q}$ follows the path in figure 4.1.

4.4 t-U-Model

The t-U-Model is the simplest version of the Hubbard model. In dimensionless units it contains $\frac{U}{t}$ as the only free model parameter. The band structure is then only specified by the geometry of the lattice. In the case of a square lattice, the band structure fulfils $\varepsilon_{\mathbf{k}} = -\varepsilon_{\mathbf{k}+\mathbf{Q}}$. By this relation, the energies $E^{\pm}$ of the new bands reduce at half filling to a much simpler form,

$$E^{\pm}_{\mathbf{k},\sigma} = \pm\sqrt{\varepsilon^2_{\mathbf{k}} - U^2 m^2_{s,\sigma}}. \tag{4.9}$$

The energies along the path through the previously defined Brillouin zone are shown in figure 4.4. The two bands are split by a gap of width Um_s. They are completely symmetric with respect to the Fermi surface and the energy along the boundary of the reduced Brillouin zone S-X is constant.

Such a model was used by Peres and Araújo [4] to calculate the spin wave dispersion of La_2CuO_4, the cuprate analogue to Sr_2IrO_4. They could successfully reproduce the spin wave dispersion measured by inelastic neutron scattering. The parameters found were $t_{\text{cup}} = 0.295\text{eV}$ and $U_{\text{cup}} = 6.1 \cdot t_{\text{cup}} = 1.8\text{eV}$. We use their calculation scheme and adjusted it to the specifications found in Sr_2IrO_4. In the first approach we use the same simple one parameter band structure, based on nearest neighbour hopping only.

The spin wave dispersions of both materials show a very similar qualitative behaviour. The most characteristic difference is the dispersion along the boundary of the reduced Brillouin zone, e.g. the line S-X in figure 4.1. The ratio of

frequencies at S and X,

$$r = \frac{\omega(\frac{1}{4}, \frac{1}{4})}{\omega(\frac{1}{2}, 0)}. \tag{4.10}$$

provides a quantitative measure of this effect. In La_2CuO_4 the experimentally measured ratio is relatively large with an value of $r = 0.85$, compared to $r = 0.54$ in Sr_2IrO_4.

The ratio r increases with U and reaches eventually $r = 1$ in the Heisenberg limit, where the dispersion is constant along the line S-X.

The Heisenberg model with nearest neighbour couplings corresponds to an expansion up to first order in $\frac{t}{U}$ only, i.e. only terms proportional to $\frac{t^2}{U}$ are taken into account. As we lower the interaction strength, higher order terms become more important. The Heisenberg model can give a lower value for r only if interactions between further neighbours are introduced. They arise from hopping processes over multiple sites, which gives a prefactor proportional to $t\cdot(\frac{t}{U})^n$ for $n+1$ hopping processes. Expanding to third order yields the Heisenberg Hamiltonian with further neighbour coupling and ring exchange, namely

$$\begin{aligned}\hat{H} = & J \sum_{\langle i,j \rangle} \mathbf{S}_i \cdot \mathbf{S}_j + J' \sum_{\langle\langle i,j \rangle\rangle} \mathbf{S}_i \cdot \mathbf{S}_j \\ & + J' \sum_{\langle\langle\langle i,j \rangle\rangle\rangle} \mathbf{S}_i \cdot \mathbf{S}_j \\ & + J_c \sum_{\langle i,j,k,l \rangle} ((\mathbf{S}_i \cdot \mathbf{S}_j)(\mathbf{S}_k \cdot \mathbf{S}_k) + (\mathbf{S}_i \cdot \mathbf{S}_l)(\mathbf{S}_k \cdot \mathbf{S}_j) - (\mathbf{S}_i \cdot \mathbf{S}_k)(\mathbf{S}_j \cdot \mathbf{S}_l))\end{aligned} \tag{4.11}$$

The couplings are given by [18]

$$J = 4\frac{t^2}{U} - 24\frac{t^4}{U^3}; \qquad J' = J'' = 4\frac{t^4}{U^3}; \qquad J_c = 80\frac{t^4}{U^3}. \tag{4.12}$$

Primes denote second and third neighbours respectively. The index c stands for cyclic exchange, i.e. hopping of a particle over four sites such that it ends up at the site where it started. where the labels $\langle i, j, k, l \rangle$ in the last sum denotes a ring of four sites, that are labelled anticlockwise. Especially the ring exchange seems to contribute to the dispersion along the zone boundary [19]. It can be absorbed in the neighbour exchange couplings. In the spin-$\frac{1}{2}$ case the relations are

$$J_{\text{eff}} = J - \frac{1}{2}J_c, \qquad J'_{\text{eff}} = J' - \frac{1}{4}J_c, \tag{4.13}$$

while the third neighbour exchange J'' remains unchanged.

We found that the Hubbard model based on nearest neighbour hopping only is not capable of describing the dispersion observed in experiments. Choosing $U = 4.7 = 1.2\text{eV}$ provides the best description of the spin wave dispersion along most parts of the path. A comparison with measurements can be seen in figure

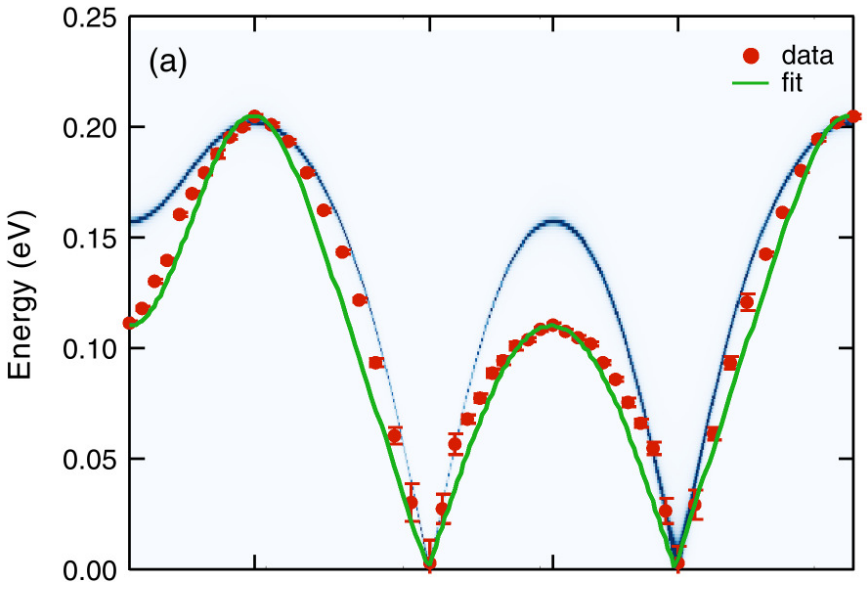

Figure 4.5: Renormalized spin wave dispersion for the t-U-model, $U = 4.7$ (blue). Graphs for RIXS measurements (red) and J-J'-J''-fit (green) are token from [20] and were recoloured. The exchange couplings J, J' and $J^7\!/\!/$ are treated there as independent parameter and do not follow the relations to U and t.

4.5. The spin wave velocity at $c = \frac{\mathrm{d}\omega}{\mathrm{d}\mathbf{k}}\big|_{\mathbf{k}=0}$ is well described after renormalization as described in chapter 3.2.2. With the same renormalization factor the dispersion along the zone boundary of the whole Brillouin zone, namely from X to M, is represented at a high level of agreement. The model fails however to catch the lowered dispersion around $\mathbf{q} = (\frac{1}{4}, \frac{1}{4})$. The calculated dispersion is way to high, giving us a ratio of $r = 0.8$. It is possible to get to lower values of r for smaller U, but the resulting dispersion fails then to match the spin wave velocity and the total energy scale. An value for r as low as the one found in the iridates will not be reached in this model for any value of U above the critical value of an metal-insulator transition.

In addition to the excitations, where ω has a clear functional dependence on $\mathbf{q}$, we find an area of continuous excitations, as can be seen in figure 4.6. We show the contributions of the longitudinal (χ^{zz}) and transversal (χ^{+-}) component of the susceptibility separately. This reveals that the spin wave dispersion at lower energies is determined by χ^{+-} completely. while contributions from χ^{zz} to the excitation spectrum lie solely in the continuum, as can be seen from. Excitations in the longitudinal direction are only possible, when the anti-ferromagnetic ordering of the ground state is distorted, which comes with a energetic cost, that increases with U.

The continuum begins at energies, comparable to the band gap between $E^+_{\mathbf{k}}$

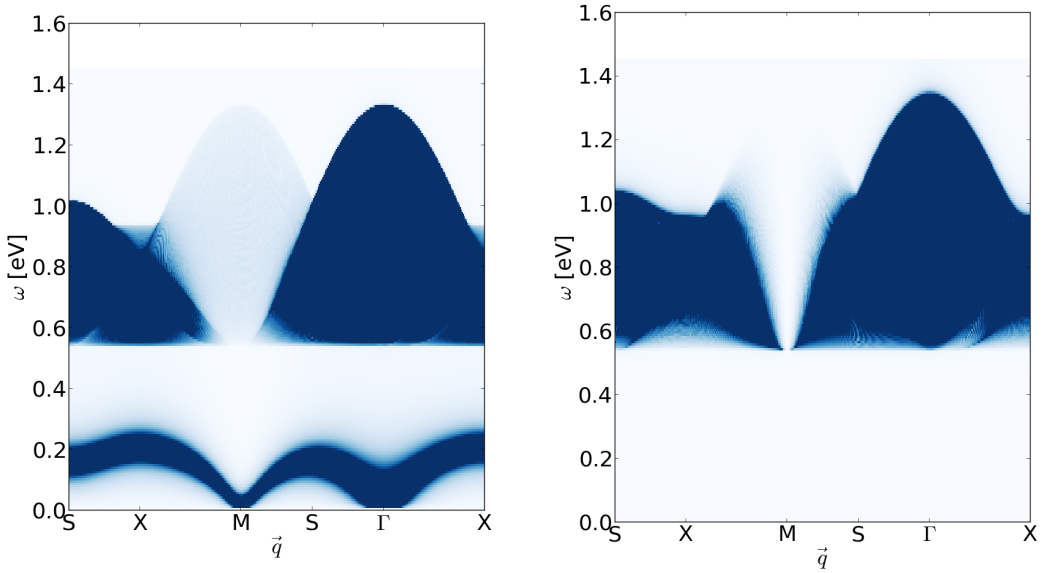

(a) transversal susceptibility χ^{+-}

(b) longitudinal susceptibility χ^{zz}

Figure 4.6: Transversal and longitudinal component of χ in the t-U-model for $U = 4.7t$, including the continuum at higher energies ω. The intensity was truncated at the same value for both pictures and such, that the lower intensities of the continuum are clearly visible.

and $E^-_{\mathbf{k}}$ and stretches mainly over an area of two times the band width of $E^{\pm}_{\mathbf{k}}$. for the t-U-model the continuum begins at 0.54eV for $U = 4.7$. Around the critical value U_c, continuum excitations merge with the spin wave excitations. In experiments a large gap is found between the low energy excitations and the continuum, which indicates a U well above the critical value [20].

This continuum corresponds to the excitation of an electron into the otherwise unoccupied upper energy band $E^+_{\mathbf{k}}$. The emergence of the continuum can be inferred from the mathematical expression of χ. In calculating bubble diagrams, one encounters sums over terms like $(E^-_{\mathbf{p}} + \omega - E^+_{\mathbf{p}+\mathbf{q}})^{-1}$. They are suppressed by a factor of $(1 + \mathrm{e}^{E^-_{\mathbf{k}} T})^{-1}$, but for ω larger than the band gap, but lower than the maximum difference between the bands, their denominator vanishes for certain ω and they can give a big contribution to the sum over such expressions for different momenta. In experiment the measured continuum begins around 0.5eV [19], which is of the same magnitude, but less then the lower bound found in our calculations based on the t-U-model. Furthermore, the lower bound of continuous excitations is not a straight line as it is in our calculations. This indicates that the model is to much simplified and missing therefore some essential features. At these energy scales there are further excitations possible, for example excitations to the $J = \frac{3}{2}$ states, which are not covered by our calculation scheme.

4.5 t-t'-t''-U-Model

In the previous chapter we saw that an approach with only nearest neighbour interactions is not capable of reproducing all the observed features in the magnetic excitations of Sr_2IrO_4. In order to improve our model, we extend the band structure beyond nearest neighbour hopping by introducing second and third neighbour hopping terms. This provides a more realistic description of the system and even though the parameters are small compared to t, they are needed in order to correctly reproduce the measured spin wave dispersion.

The hopping parameters t, t', t'' were treated as fixed external parameters. This means they were taken from first principle calculations done by Wang and Senthil [20] rather than adjusted to experiments. We use again t as the basic energy unit and express other parameters in terms of it. There are therefore two new parameters entering the calculations, the ratios t'/t and t''/t, which will be denoted by t' and t'' in the following discussion. Normalizing the energy scale to t reduces not only the number of parameters, it is also easier to find the ratio of neighbour interactions from calculations. In order to get absolute values, one needs to adjust the energy scale of the resulting dispersion to a known absolute value of the band [21].

The values from [20] are based on fits to a multi orbital tight binding model that include all the t_{2g} states together with the hybridization with the p orbitals from the ligands. The couplings between these orbitals were then fitted to repro-

t	t'	t''
0.258eV	0.06eV	0.03eV
1	0.2326	0.1163

Table 4.1: Hopping parameters for the band structure in the t-t'-t''-U-model [20]. The second line contains the relative values, normalized to t.

duce the band dispersion that was calculated in the linear density approximation (LDA) including SOC. After a projection to the spin-$\frac{1}{2}$ subspace, we get the effective couplings of between sites in our one orbital Hubbard model. The values used in this thesis were With those parameters the band structure of the square lattice is

$$\varepsilon_{\mathbf{k}} = -2t\left(\cos k_x + \cos k_y\right) - 4t' \cos k_x \cos k_y - 2t''\left(\cos 2k_x + \cos 2k_y\right) \qquad (4.14)$$

as explained in chapter 2.5.

The second and third neighbour hopping parameters are substantially smaller than t, but big enough to change the results significantly. The most important feature is the removal of the degeneracy in $E^{\pm}_{\mathbf{k}}$ along the border of the reduced Brillouin zone. This was the main reason, why the t-U-model was not capable of reproducing the spin wave dispersion. In figure 4.7 we plotted again the energies of $E^{\pm}_{\mathbf{q}}$ along the same path as before. The gap between the upper and lower band is smaller than in the previous case, where it was given by Um_s. At the same time the bands stretch over a larger energy range.

The t-t'-t''-U-Hubbard model is capable of describing all features of the measured dispersion to a high level of agreement. The optimal value for the Hubbard interaction was found to be $U = 4.4 = 1.1eV$. The value was optimized in several trials by guidance of the eye, until the experimental values were met. With the renormalization due to quantum fluctuations a very high level of agreement could be achieved, see figure 4.8. Again, the spin wave velocity and the dispersion along X-M and Γ-X is very well described. The ratio r of energies at $\mathbf{q} = (\frac{1}{4}, \frac{1}{4})$ and $(\frac{1}{2}, 0)$ is slightly overestimated. At $\mathbf{q} = (\frac{1}{4}, \frac{1}{4})$ and in its direct vicinity the spin-wave energy is a little overestimated. This results in a larger value of r, since $\omega(\frac{1}{2}, 0)$ is matched exactly. We get $r =$ which overestimates the measured value by 5%. The derivation is small compared to the uncertainties in the measured spin-wave energies.

The staggered magnetization at $U = 4.4$ is $m_s = 0.73$ according to Eq. (3.12). As mentioned above, there is a net ferromagnetic moment proportional to the anti-ferromagnetic ordering parameter m_s, because of the canted orientation of the oxygen octahedra. We found for the magnetic ordering parameter $m = m_s \sin\Theta = 0.139$. It is related to the total magnetic moment by the magnetic

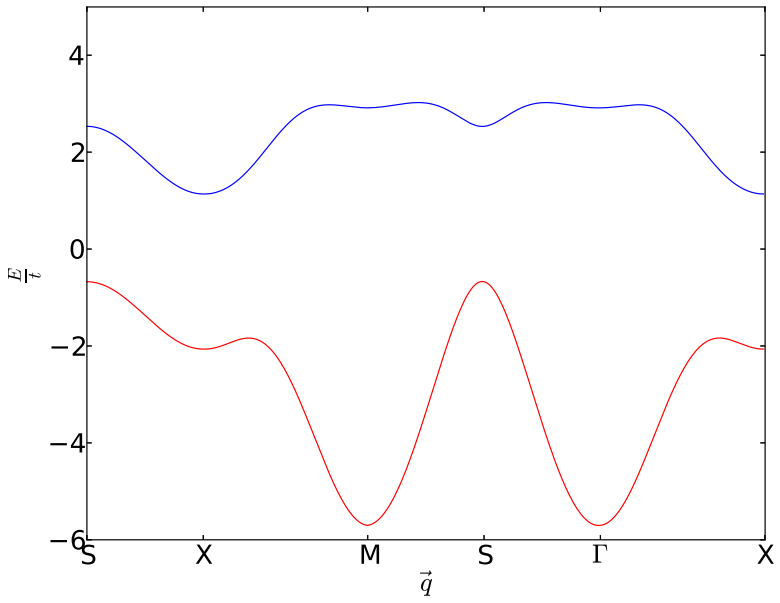

Figure 4.7: $E^{\pm}_{\mathbf{q}}$ in the extended model that includes second and third neighbour hopping terms. U was chosen to be $4.4t$, $\mathbf{q}$ follows the path through the Brillouin zone described in figure 4.1.

moment of a single site, that is defined as $g\mu_b J$. The observed ferromagnetic moment is $0.14\mu_b$ [22]. Our result is therefore in good agreement, given the magnetic moment of $1\mu_b$ at each Ir site, which is the value of the atomic limit. The canted structure provides therefore a good explanation of the observed weak ferromagnetic moment in an anti-ferromagnetic ground state.

Another quantity, that is closely related to the Hubbard-U is the width of the Mott gap. The Mott gap is the split of the $J = \frac{1}{2}$-band due to the repulsive Hubbard interaction into the bands denoted by $E^{\pm}_{\mathbf{k}}$ respectively. With the optimal value of U found in our calculation and the corresponding staggered magnetization m_s, the width of the band gap is given by $\Delta_{\text{Mott}} = 1.6t = 0.47\text{eV}$. This is close to, but slightly lower than the experimental result of 0.54eV at $T = 10\text{K}$, as found through optical spectroscopic measurements by Moon et al. [23].

With the changed dispersion the continuous excitations at higher energies agree with experiments on a qualitative level. The calculated dispersion is compared to the measured one in 4.9. Due to the changed energy bands, our result shows no longer a constant boundary at the lower end, but displays $\mathbf{k}$-dependence as well. A quantitative comparison of the excitations is difficult, since the experimental data contains spin orbit excitations as well. Those lie in the centre of the continuous band. On a qualitative level we note that the bulges at the low energy end of the continuum appear for the same momenta as in the measurements. The

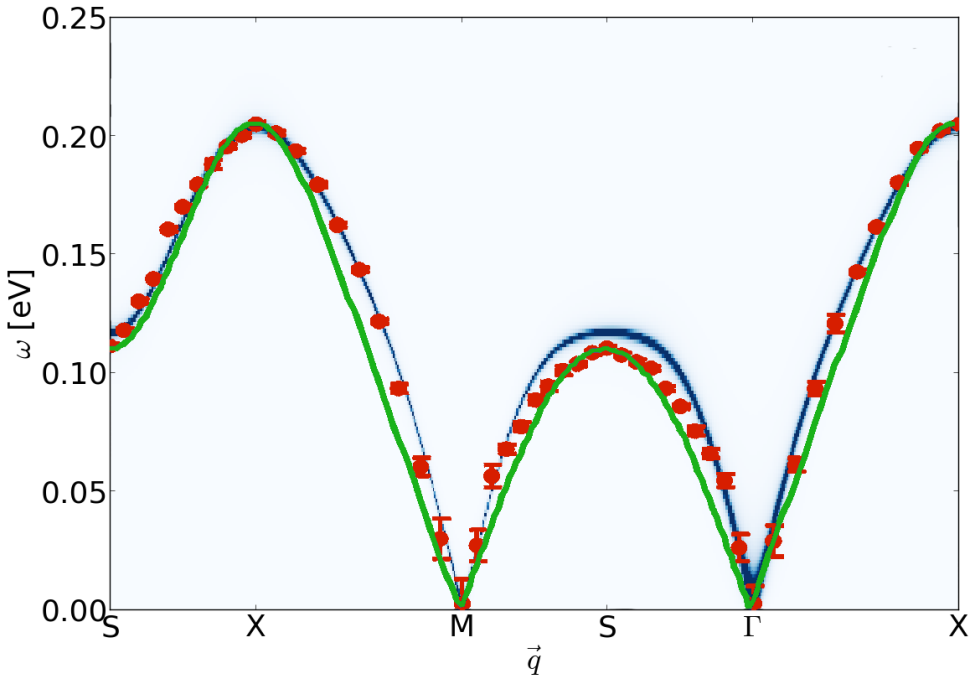

Figure 4.8: Spin-wave dispersion for $\frac{U}{t} = 4.4$ for the t-t'-t'-U-Hubbard model (blue) compared to measurements (red) and a up to third neighbour Heisenberg model (green). Experimental values and Heisenberg fit are taken from [8] and recoloured.

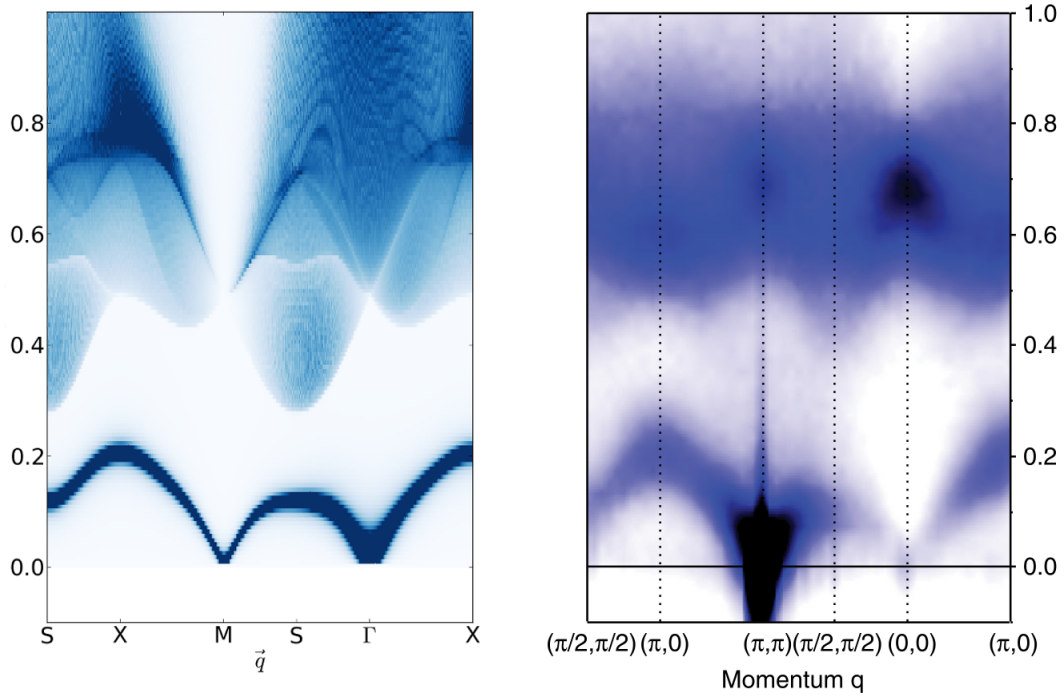

(a) calculated spin wave dispersion for $U = 4.4$.

(b) measured excitations, taken from [8]

Figure 4.9: comparison of the excitation spectrum form our calculations and RIXS measurements. The energy scale in both graphs is given in eV. The measured excitations contain also spin orbit excitations between 0.4eV and 0.8eV

lowest excitations are found at $\mathbf{q} = (\frac{1}{4}, \frac{1}{4})$. This is the momentum transfer that connects the $\mathbf{k}$ for the highest value of $E^-_{\mathbf{k}}$ with the momentum, where $E^+_{\mathbf{k}}$ is minimal, as one would expect for such excitations.

Kim et al. [8] did not only measure the inelastic scattering cross section, they provided also a model to describe the data. Their model is the Heisenberg model with up to third neighbour couplings, with the parameters J, J' and J'' for the first, second and third neighbour exchange couplings respectively, without an parameter for cyclic exchange. All three parameters were treated as free parameters and fitted to the measured spin wave dispersion. The values were found to be $J = 60\text{meV}$, $J' = -20\text{meV}$ and $J'' = 15\text{meV}$. The resulting dispersion reproduces the right energies at the points X and S and therefore the right r as well, while the energies along the path connecting these points are systematically underestimated.

In an effective model the effect of cyclic exchange can be absorbed in the other parameters. J and J' will be lowered by that, while J'' remains unchanged. As an expansion of the Hubbard model, these parameters are related through their dependence on t, t', t'' and U. Up to second order, they are given by

$$\begin{aligned} J &= 4\frac{t^2}{U} - 64\frac{t^4}{U^3} = 41\text{meV} , \qquad J' = 4\frac{t'^2}{U} - 16\frac{t^4}{U^3} = -38\text{meV} \\ J'' &= 4\frac{t''^2}{U} + 4\frac{t^3}{U^4} = 15\text{meV}. \end{aligned} \tag{4.15}$$

where we have inserted the values found above for U and t, t', t'' from table 4.1. These values do not agree very well with the fit and show that their parameters do not follow the functional dependence on the parameters of the Hubbard model. Also our Hubbard model fit describes the dispersion with a higher accuracy. At the same time it has just one free parameter, while the other parameters can be obtained by first principle calculations.

Our optimal value for $U = 4.4$ corresponding to 1.1eV is substantially lower than the one found in the similar cuprate compounds. In the cuprates U is usually set to around $7t_{\text{Cu}}$ for the corresponding $t_{\text{Cu}} = 0.3\text{eV}$ [4]. This is expected, since the $5d$ orbitals are more extended, which reduces the intra orbital interaction. In the literature the Hubbard interaction is often estimated to be $U = 2\text{eV}$ in iridates [10]. Our calculations shows that the interaction is weaker and $U = 1.1\text{eV}$ yields a more realistic description of the system. With this value of U and its SOC strength, Sr_2IrO_4 is still in the anti-ferromagnetic phase, but close to the transition point to a paramagentic metal [11].

4.6 Outlook

We showed using the example of Sr_2IrO_4 that the one band Hubbard model in the mean field treatment works well as an effective model for correlated systems

with strong spin orbit coupling. Using previously calculated band structure parameters we introduced the Hubbard interaction and fixed its strength, the only free parameter in the model, by comparison to experiment. We could show how hopping terms beyond the nearest neighbours are necessary to describe the observed dispersion. The model reproduced the spin wave dispersion very well after introducing a constant renormalization factor. Furthermore, it gave a realistic sketch of the continuum at higher energies. We found a value of $U = 1.1eV$, which is lower than the one usually assumed in the literature. The value is close to the metal-insulator transition point, but clearly in the insulating phase. Furthermore the model provides an explanation for the value of the charge gap and yields the correct ferromagnetic moment of this material.

There is room for improvement in the analysis of the susceptibility. One could take not only the position of the poles into account, but also quantify their height and broadness, making a more precise comparison to experiment possible. We found corrections due to quantum fluctuations necessary to include and that the most important contribution of spin wave velocity renormalization is momentum independent. It might however be worth to develop a more elaborate way of calculating corrections in the Hubbard model itself refining thereby the Greens functions itself.

In further work this model can be extended to other crystals with antiferromagnetic ordering like the other elements of the Ruddelson-Popper series, namely $SrIrO_3$ and the bilayer iridate $Sr_3Ir_2O_7$. The different geometric set-up gives a different band structure due to changed geometry and hopping parameters. It can be further improved by introducing hopping between layers, which will be more important in multi-layered iridates. The calculation scheme might also be used for honeycomb lattices such as for example Na_2IrO_3.

Another interesting application for this type of calculation is the doped case, e.g. a filling factor that is shifted away from $n = 1$. It is yet an open question, if iridates can be doped such that they show superconductivity as found in the cuprates and understanding the doped case could shed light on this question from a theoretical point of view.

Appendix A

Matsubara Frequency Summation

In the calculations above we encounter functions of the type $\sum_{n\in\mathbb{Z}} f(\mathrm{i}\omega_n)$. f is usually a propagator or a function of propagators. We require F to vanish fast at infinity, that is $|f(z)| < \frac{1}{z} \to 0$ for $|z| \to \infty$ The Matsubara frequencies can be fermionic or bosonic, depending on the type of operator they describe. For $n \in \mathbb{Z}$ they are given by

$$\mathrm{i}\omega_n = \begin{cases} (2n+1)\mathrm{i}\frac{\pi}{\beta} & \text{(fermionic)} \\ 2n\mathrm{i}\frac{\pi}{\beta} & \text{(bosonic)} \end{cases} \tag{A.1}$$

The Matsubara frequencies are the poles of the function

$$h(z) = \frac{\beta}{\mathrm{e}^{\beta z} \pm 1} \tag{A.2}$$

with the positive sign for fermions and the negative one for bosonic frequencies. Using Cauchy's integral theorem, we can express the sum over the frequencies as an integral. We choose a contour γ_1 that encloses the imaginary axis counterclockwise in a way, that it avoids any other poles not on the axis, see figure A.1. This means running parallel to the axis on a very small distance and closing it at infinity.

We can now blow up this contour to a circle with infinite radius which we shall call γ_2. Since the function vanishes fast, the integral will be 0, but we have to pick up the Residual of every pole we encounter in deforming the contour. The poles will be encircled clockwise, which gives rise to a minus sign. In doing

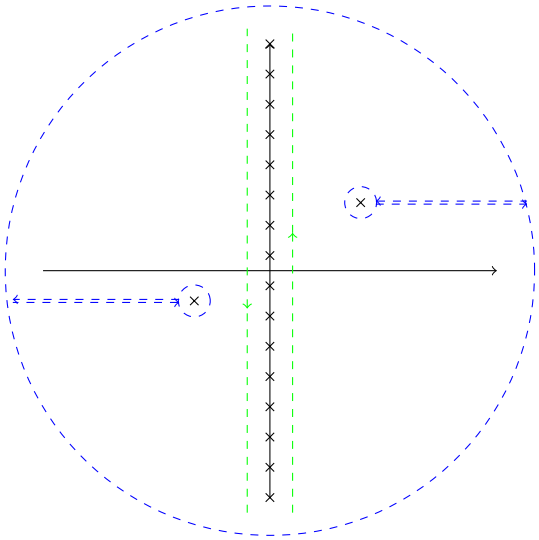

Figure A.1: Contour γ_1 (green) enclosing the poles close to the axis, γ_2 (blue) at infinite radius, but encircling the poles not on the imaginary axis.

so, we get the relation

$$\begin{aligned}\sum_{n\in\mathbb{Z}} f(\mathrm{i}\omega_n) &= \frac{1}{2\pi\mathrm{i}} \oint_{\gamma_1} \mathrm{d}z\, f(z)\cdot h(z) \\ &= \frac{1}{2\pi\mathrm{i}} \underbrace{\oint_{\gamma_2} \mathrm{d}z\, f(z)\cdot h(z)}_{=0} - \sum_i f(z_i)\cdot h(z_i) \qquad \text{(A.3)} \\ &\text{for } i \in \{z\in\mathbb{C} | z \text{ pole of} f\}\end{aligned}$$

The functions used here usually have poles on the real axis. With choosing the contour close enough to the imaginary axis we keep those outside of the enclosed area. For functions falling off faster than $\frac{1}{|z|^{1+\delta}}$ $(\delta > 0)$ as $|z| \to \infty$ we can blow up the contour to a circle with infinite radius. The integral will vanish, but we pick up residuals for every pole of f. In total we get

$$\sum_{n\in\mathbb{Z}} f(\mathrm{i}\omega_n) = \frac{1}{2\pi\mathrm{i}} \int_0 \mathrm{d}z f(z) \frac{\beta}{1+\mathrm{e}^{\beta z}} = \sum_{\mathrm{Res}_f} \left.\frac{f(z)\beta}{1+\mathrm{e}^{\beta z}}\right|_{z=z_{\mathrm{Res}_f}} \qquad \text{(A.4)}$$

Bibliography

[1] J.G. Bednorz and K.A. Müller. Possible high t_c superconductivity in the ba-la-cu-o system. *Zeitschrift für Physik B Condensed Matter*, 64(2):189–193, 1986. ISSN 0722-3277. doi: 10.1007/BF01303701. URL http://dx.doi.org/10.1007/BF01303701.

[2] J.M. Longo, P.M. Raccah, and J.B. Goodenough. Pb2m2o7-x (m = ru, ir, re) - preparation and properties of oxygen deficient pyrochlores. *Materials Research Bulletin*, 4(3):191 – 202, 1969. ISSN 0025-5408. doi: http://dx.doi.org/10.1016/0025-5408(69)90056-7. URL http://www.sciencedirect.com/science/article/pii/0025540869900567.

[3] Hiroshi Watanabe, Tomonori Shirakawa, and Seiji Yunoki. Theoretical study of insulating mechanism in multiorbital hubbard models with a large spin-orbit coupling: Slater versus mott scenario in sr_2iro_4. *Phys. Rev. B*, 89: 165115, Apr 2014. doi: 10.1103/PhysRevB.89.165115. URL http://link.aps.org/doi/10.1103/PhysRevB.89.165115.

[4] N. M. R. Peres and M. A. N. Araújo. Spin-wave dispersion in La_2CuO_4. *Phys. Rev. B*, 65:132404, Mar 2002. doi: 10.1103/PhysRevB.65.132404. URL http://link.aps.org/doi/10.1103/PhysRevB.65.132404.

[5] Anatole Abragam and Brebis Bleaney. *Electron Paramagnetic Resonance Of Transition Ions*. The International Series Of Monographs On Physics. Clarendon Press, Oxford, 1970.

[6] Perovskite - crystal structure, 2014. URL http://mrc.iisc.ernet.in/Research_Areas/01_Perovskite.htm.

[7] M. K. Crawford, M. A. Subramanian, R. L. Harlow, J. A. Fernandez-Baca, Z. R. Wang, and D. C. Johnston. Structural and magnetic studies of Sr_2IrO_4. *Phys. Rev. B*, 49:9198–9201, Apr 1994. doi: 10.1103/PhysRevB.49.9198. URL http://link.aps.org/doi/10.1103/PhysRevB.49.9198.

[8] Jungho Kim, D. Casa, M. H. Upton, T. Gog, Young-June Kim, J. F. Mitchell, M. van Veenendaal, M. Daghofer, J. van den Brink, G. Khaliullin,

and B. J. Kim. Magnetic excitation spectra of Sr_2IrO_4 probed by resonant inelastic x-ray scattering: Establishing links to cuprate superconductors. *Phys. Rev. Lett.*, 108:177003, Apr 2012. doi: 10.1103/PhysRevLett.108.177003. URL http://link.aps.org/doi/10.1103/PhysRevLett.108.177003.

[9] Michael Tinkham. *Group Theory And Quantum Mechanics*. McGraw-Hill Book Company, 1964.

[10] Hosub Jin, Hogyun Jeong, Taisuke Ozaki, and Jaejun Yu. Anisotropic exchange interactions of spin-orbit-integrated states in sr2iro4. *Phys. Rev. B*, 80:075112, Aug 2009. doi: 10.1103/PhysRevB.80.075112. URL http://link.aps.org/doi/10.1103/PhysRevB.80.075112.

[11] Hiroshi Watanabe, Tomonori Shirakawa, and Seiji Yunoki. Microscopic study of a spin-orbit-induced mott insulator in ir oxides. *Phys. Rev. Lett.*, 105:216410, Nov 2010. doi: 10.1103/PhysRevLett.105.216410. URL http://link.aps.org/doi/10.1103/PhysRevLett.105.216410.

[12] R.C. Albers, N.E. Christensen, and A. Svane. Hubbard-u band-structure methods. *Journal of Physics: Condensed Matter*, 21, 2009. doi: 10.1088/0953-8984/21/34/343201. URL http://iopscience.iop.org/0953-8984/21/34/343201.

[13] F. Baumberger, N. J. C. Ingle, W. Meevasana, K. M. Shen, D. H. Lu, R. S. Perry, A. P. Mackenzie, Z. Hussain, D. J. Singh, and Z.-X. Shen. Fermi surface and quasiparticle excitations of sr2rho4. *Phys. Rev. Lett.*, 96:246402, Jun 2006. doi: 10.1103/PhysRevLett.96.246402. URL http://link.aps.org/doi/10.1103/PhysRevLett.96.246402.

[14] Alexander Altland and Ben D Simons. *Condensed matter field theory*. Cambridge University Press, 2010.

[15] C. M. Canali, S. M. Girvin, and Mats Wallin. Spin-wave velocity renormalization in the two-dimensional heisenberg antiferromagnet at zero temperature. *Phys. Rev. B*, 45:10131–10134, May 1992. doi: 10.1103/PhysRevB.45.10131. URL http://link.aps.org/doi/10.1103/PhysRevB.45.10131.

[16] Avinash Singh. Quantum corrections in an antiferromagnet: A systematic diagrammatical treatment of the hubbard model. *Phys. Rev. B*, 43:3617–3625, Feb 1991. doi: 10.1103/PhysRevB.43.3617. URL http://link.aps.org/doi/10.1103/PhysRevB.43.3617.

[17] Jean-Michel Carter, Vijay Shankar V., and Hae-Young Kee. Theory of metal-insulator transition in the family of perovskite iridium oxides. *Phys. Rev. B*, 88:035111, Jul 2013. doi: 10.1103/PhysRevB.88.035111. URL http://link.aps.org/doi/10.1103/PhysRevB.88.035111.

[18] M Takahashi. Half-filled hubbard model at low temperature. *Journal of Physics C: Solid State Physics*, 10(8):1289, 1977. URL http://stacks.iop.org/0022-3719/10/i=8/a=031.

[19] R. Coldea, S. M. Hayden, G. Aeppli, T. G. Perring, C. D. Frost, T. E. Mason, S.-W. Cheong, and Z. Fisk. Spin waves and electronic interactions in Sr_2IrO_4. *Phys. Rev. Lett.*, 86:5377–5380, Jun 2001. doi: 10.1103/PhysRevLett.86.5377. URL http://link.aps.org/doi/10.1103/PhysRevLett.86.5377.

[20] Fa Wang and T. Senthil. Twisted hubbard model for Sr_2IrO_4: Magnetism and possible high temperature superconductivity. *Phys. Rev. Lett.*, 106:136402, Mar 2011. doi: 10.1103/PhysRevLett.106.136402. URL http://link.aps.org/doi/10.1103/PhysRevLett.106.136402.

[21] A. A. Kordyuk, S. V. Borisenko, M. Knupfer, and J. Fink. Measuring the gap in angle-resolved photoemission experiments on cuprates. *Phys. Rev. B*, 67:064504, Feb 2003. doi: 10.1103/PhysRevB.67.064504. URL http://link.aps.org/doi/10.1103/PhysRevB.67.064504.

[22] G. Cao, J. Bolivar, S. McCall, J. E. Crow, and R. P. Guertin. Weak ferromagnetism, metal-to-nonmetal transition, and negative differential resistivity in single-crystal sr2iro4. *Phys. Rev. B*, 57:R11039–R11042, May 1998. doi: 10.1103/PhysRevB.57.R11039. URL http://link.aps.org/doi/10.1103/PhysRevB.57.R11039.

[23] S. J. Moon, Hosub Jin, W. S. Choi, J. S. Lee, S. S. A. Seo, J. Yu, G. Cao, T. W. Noh, and Y. S. Lee. Temperature dependence of the electronic structure of the jeff=12 mott insulator sr2iro4 studied by optical spectroscopy. *Phys. Rev. B*, 80:195110, Nov 2009. doi: 10.1103/PhysRevB.80.195110. URL http://link.aps.org/doi/10.1103/PhysRevB.80.195110.